Test of a New Prototype of Multiwire Proportional Chamber with Pixel Pad Cathode Readout

by

Octavian Teodorescu

A thesis submitted
to the Faculty of Graduate Studies and Research
in partial fulfillment of the requirements
of the degree of

Master of Science
in Physics

Physics Department, McGill University, Montréal, Canada.

0-612-44297-7

Abstract

A new prototype of multiwire proportional chamber (MWPC) with pixel configurated pad cathode was built as a joint effort by McGill University, Lund University and Oak Ridge National Laboratory as part of the development of the tracking system of the PHENIX detector at the Relativistic Heavy Ion Collider (RHIC). This thesis first describes the implementation of a new readout electronics for the pad chambers. In this electronics, the charge of the pads is digitized using a preamplifier/shaper/discriminator integrated CMOS chip with adjustable threshold. All chips and components are mounted on specially designed 48-channel readout cards using chip-on-board (COB) technology. Using this new readout, the performance of the pad chamber is tested with cosmic rays and X-ray source. The prototype response, efficiency and gain are measured as functions of detector operating conditions. The operation of the chamber shows a very good stability over long periods of testing. Excellent efficiencies, above 99%, are observed in tests using discriminator thresholds between $2-4\ fC$, which represents $1-1.5\%$ of the most probable anode charge produced at a normal anode voltage of $1850V$. Under this conditions, the reconstructed hit patterns are relatively small. This is leading to a very good position resolution of about half of the cell size. An excellent description of chamber behavior was obtained using Monte Carlo simulations, showing that we can use these simulations to predict and optimize the performance of such chamber.

Résumé

Un nouveau prototype de chambre proportionnelle à fils multiples (MWPC), utilisant une technologie de lecture de cathode à segmentation en pixel, a été développée en collaboration entre l'Université McGill, l'Université de Lund et le Laboratoire National de Oak Ridge. Ce travail s'inscrit dans le cadre d'un effort de recherche et développement du système de reconstitution des trajectoires de particules pour le détecteur PHENIX au collisionneur d'ions lourds relativistes (RHIC). Cette thèse descrit en premier lieu l'utilisation d'un nouveau système électronique de lecture pour les chambres à segmentation. Dans ce circuit électronique, les charges induites sur la cathode à segmentation sont numérisées en utilisant un système électronique CMOS (préamplificateur/mise en forme/discriminateur) hautement intégré et doté d'un seuil variable. Toutes les puces et autres composants électroniques sont montés sur des cartes de lecture à 48-cannaux, spécialement conçues avec la technologie de puce-sur-cir cuit (COB). En utilisant ce nouveau système de lecture, l'efficacité de la chambre à pixel a été testée à l'aide de rayons cosmiques et d'une source de rayons-X. La réponse du prototype ainsi que son rendement et son gain ont été mesuré en fonction des conditions d'opération du détecteur. Le fonctionnement de la chambre montre une tres grande stabilitée pour de longues périodes d'essais. D'excellents rendements, supérieurs à 99%, sont observés lors d'essais utilisant des seuils discriminateurs de $2 - 4\ fC$, ce qui represente de 1 - 1.5% des charges les plus probables à l'anode pour un voltage de 1850 V. Sous de telles conditions, la cible reconstituée à partir de la distribution des particules est relativement petite. Ce resultat permet d'établir une très bonne résolution spatiale de l'ordre d'une demie cellule. Une excellente description du comportement de la chambre a été obtenue par simulation utilisant des calculs Monte Carlo, ce qui permet de predire ainsi que d'optimiser les performances de telle chambre.

Contents

List of Figures

List of Tables

Acknowledgment

I would like to express my sincere thanks to my supervisor, professor Jean Barrette, for his permanent guidance and help. He taught, guided and corrected me in each step I put toward the completion of this thesis. He often amazed me by his deep understanding of the physics doubled by a great experience in the field of relativistic heavy-ions. Our discussions on topics, related or not to physics, also revealed me a man of a great character devoted to help other people. I am also grateful to him for his financial support which made possible the continuation of my studies in Canada. I will always be thankful for what I have learned from him about both physics and life.

I would also like to address special thanks to professor S. K. (Tommy) Mark who initiated, directed, and closely supervised this project. He gave me this great opportunity, to join an important project like PHENIX, and to participate in several important meetings where I met and learned from experts in the field of relativistic heavy-ions. His broad knowledge on the PHENIX project, and pad chambers in particular, were an invaluable help for me.

Many thanks to the pad chamber groups from Oak Ridge National Laboratory (headed by Mr. Bill Bryant) and Lund University (headed by Anders Oskarsson, H-A. Gustafsson and L. Osterman) who designed the readout electronic system. The Lund crew gave me a great help with the electronics implementation as well.

Special thanks to Leo Nikinnen for his permanent assistance, especially with the electronics hardware. He did not hesitate to put extra hours to help me "make things running".

Yujin Qi was a great help for me especially through his assistance with the data acquisition setup. I am also grateful to Kirill Filimonov for his constant help, mainly with the simulation software. Rainer Ullman gave me a lot of help especially related to the data analysis. Our summer student, Vincent Tabard-Cossa, gave me a great help with the drawings and proofreading of this thesis. I also acknowledge the contribution of Drs. Nick Starinski, Jan Romanski and G. S. Wang in building the prototype.

I am grateful to Daryl Borland and Ereil Fernandez for their assistance related to the mechanics hardware. I acknowledge the help I have got from the machine shop staff, especially from Steve Kecani who taught me the first steps in machining.

I will always be grateful for the moral support I have received from my loving parents, brother and friends, who have strongly encouraged me to continue my studies in Canada.

Last, but more than anything else, I am grateful for everything God has brought me. His permanent help and warm love is for me like a Sun who both enlightens and gives me spiritual warmth in this world.

Chapter 1

Introduction

The Quantum Chromodynamics (QCD) theory predicts that a new form of matter, called **Quark-Gluon Plasma (QGP)**, will be created if macroscopic volumes (nuclear size) of nuclear matter are assembled at extreme thermodynamic conditions and at energy densities (ϵ) exceeding a critical value (ϵ_c) of a few GeV/fm^3 [1]. The present thesis is related to the **P**ioneering **H**igh **E**nergy **N**uclear **I**nteraction e**X**periment (PHENIX) at the Relativistic Heavy Ion Collider (RHIC), which is being constructed at Brookhaven National Laboratory (BNL). The goals of PHENIX are to investigate the QGP prediction of a de-confined high-energy phase of matter and to search for the QGP exploring the physics of this new state of matter.

1.1 Physics Motivation

When it comes into operation RHIC will be the highest energy heavy-ion accelerator in the world, providing proton beams of center of mass (c.m.) energy 500 GeV and gold nuclear beams of c.m. energy 200 GeV/nucleon. For the first time in history, RHIC will provide the opportunity to create a baryon-free high-energy region over an extended volume of a few hundred fm^3 in a laboratory. The energy density expected to be reached in induced heavy-ion collisions at RHIC is at least 3 GeV/fm^3. QCD

theory predicts that in this conditions the quarks and gluons will lose their allegiance to specific hadrons [2]. This will lead to a phase transition toward a new form of matter (Quark-Gluon Plasma).

The production of lepton pairs (dielectron and dimuons), photons and hadrons are believed to carry the best potential signatures of QGP [3]. One of the PHENIX plans is to measure the production of these physics quantities as function of the energy density. According to Bjorken [4] the critical energy can be expressed as:

$$\epsilon_c = \frac{1}{\pi R_\perp^2 \tau_0} \frac{dE_T}{dy} = \frac{1}{\pi R_\perp^2 \tau_0} \sqrt{< p_T^2 > + m_\pi^2} \frac{dN_\pi}{dy}$$

where $N_\pi = N_{\pi^+} + N_{\pi^0} + N_{\pi^-}$ is the multiplicity of produced pions. R_T is the transverse radius of the fireball. y is the rapidity [5] and dE_T/dy is the rapidity density of transverse energy E_T. p_T is the transverse momentum, and τ_0 is estimated to be $1 fm/c$ (c = speed of light).

Since dileptons interact only electromagnetically with matter their mean free path is large compared to the size of the system formed in these collisions; therefore once produced, they can leave the interaction region and reach the detectors without further interaction, carrying information about the conditions and properties of the matter at the time of their production [6].

Dileptons can be emitted throughout the entire collision. Various processed are involved, and to the extent that they have distinct characteristics, a careful analysis should be in principle able to disentangle the whole space-time evolution of the collision [7].

The measurement of the continuum dilepton spectrum is sensitive to the initial state of the thermal system produced in the collision [8]. The number of lepton pairs emitted depends upon the product of the quark and antiquark number densities, appropriately summed over their relative momentum distributions and the thermal history of the plasma. The rate of production of pairs, primarily via quark-antiquark ($q\overline{q}$) fusion, should be proportional to the square of the rapidity distribution: $(dN/dy)^2$.

A strong dependence on temperature would imply that emission is favored at the early stages of the collision, before expansion and consequent cooling [9]. The pair p_T distribution is thus a measure of the initial temperature.

Once the system reaches thermal equilibrium, dileptons are emitted as thermal radiation during the expansion and cooling phase up to the freeze-out time when hadrons cease to interact. Thermal radiation is a good way to diagnose the plasma formed. the conjunctured QGP or a high-energy hadron gas. The relative strength of the elementary processes involved. $q\bar{q}$ annihilation in the QGP phase and $\pi^+\pi^-$ annihilation in hadron gas phase. is expected to be different [7]

The vector mesons $\rho.\omega$ and ϕ. measured through their l^+l^--decay channels. are also considered as important messengers of the collision dynamics. Specially ρ-meson was proposed as a potential signal of the restoration of chiral symmetry [10. 11] which is expected to occur at conditions similar to those leading to deconfinement [12]. Its mass and width are expected to be strongly modified as the system approaches chiral restoration. Due to its very short lifetime of 1.3 fm/c. the decay $\rho \rightarrow l^+l^-$ will occur inside the dense matter and the dilepton mass spectrum may indicate a phase transition. The short lifetime also offers an attractive possibility; several generations of ρ-mesons could be produced during the lifetime of the system. As a result the ρ-yield will increase relative to ω and could serve as a clock to measure the fireball lifetime [13].

The rate and shape of the photon spectrum contain information about the collision at distances or time scales of the order $1/p_T$. At high transverse momentum ($p_T > 5\ GeV/c$) the photons originate mostly from the initial hard collisions of the constituents (quarks and gluons) of the colliding beam. The measurement of these photons tests the quantitative understanding of the initial state of the collision and yields information about gluon structure functions in nuclei. At intermediate values of p_T ($2 < p_T < 5\ GeV/c$) photons originate mostly from the pre-equilibrium phase of the collision [14]. This production yields information about equilibration times, absorption of mini-jets, and transition from perturbative to non-perturbative phenomena. At lower momenta ($0.5 < p_T < 2\ GeV/c$) the photon spectrum should be dominated by radiation from thermalized plasma and from initial part of the hadronic phase [8]. Below 1 GeV/c a long lived mixed phase is expected in case of a first order phase transition leading to a significant radiation at the critical temperature T_C. A measurement of the photon spectrum will give direct information on T_C and life time of the mixed phase, which is connected to the difference in entropy of the plasma and hadronic phase.

On the other hand, studies of charged hadrons provide important information about the collision environment and its development in space and time. An important issue to verify the predictions is the degree of stopping expected in the central region. A simple way to measure this is the $\bar{p}/p$ ratio at zero rapidity. since this quantity is determined by the net baryon density, which is of critical importance to theoretical description of the stopping power [15]. The inclusive distributions of $\pi^+, \pi^-, K^+, K^-, p$ and $\bar{p}$ will be measured by PHENIX. Particle spectra at low and moderate p_T may yield information on the temperature of the system at freeze-out. The space-time evolution of the collision is also studied by two-boson Hanbury-Brown-Twiss (HBT) correlations. Both $\pi\pi$ and KK correlations are important because of their different contributions from resonance decays and different decoupling times from the hadronic gas.

1.2 The PHENIX Detector

The PHENIX detector consist of many subsystems of detectors divided into two central arms and two muon spectometers as end caps (see figure 1.1). Each central arm subtends 90^o in azimuth (ϕ) and ± 0.35 units in pseudorapidity (η), roughly equivalent to a polar angle (θ) acceptance of $\pm 20^o$ centered at $\theta = 90^o$. The solid angle of each arm is 0.94 sr. A number of detector systems will be needed to cover the entire

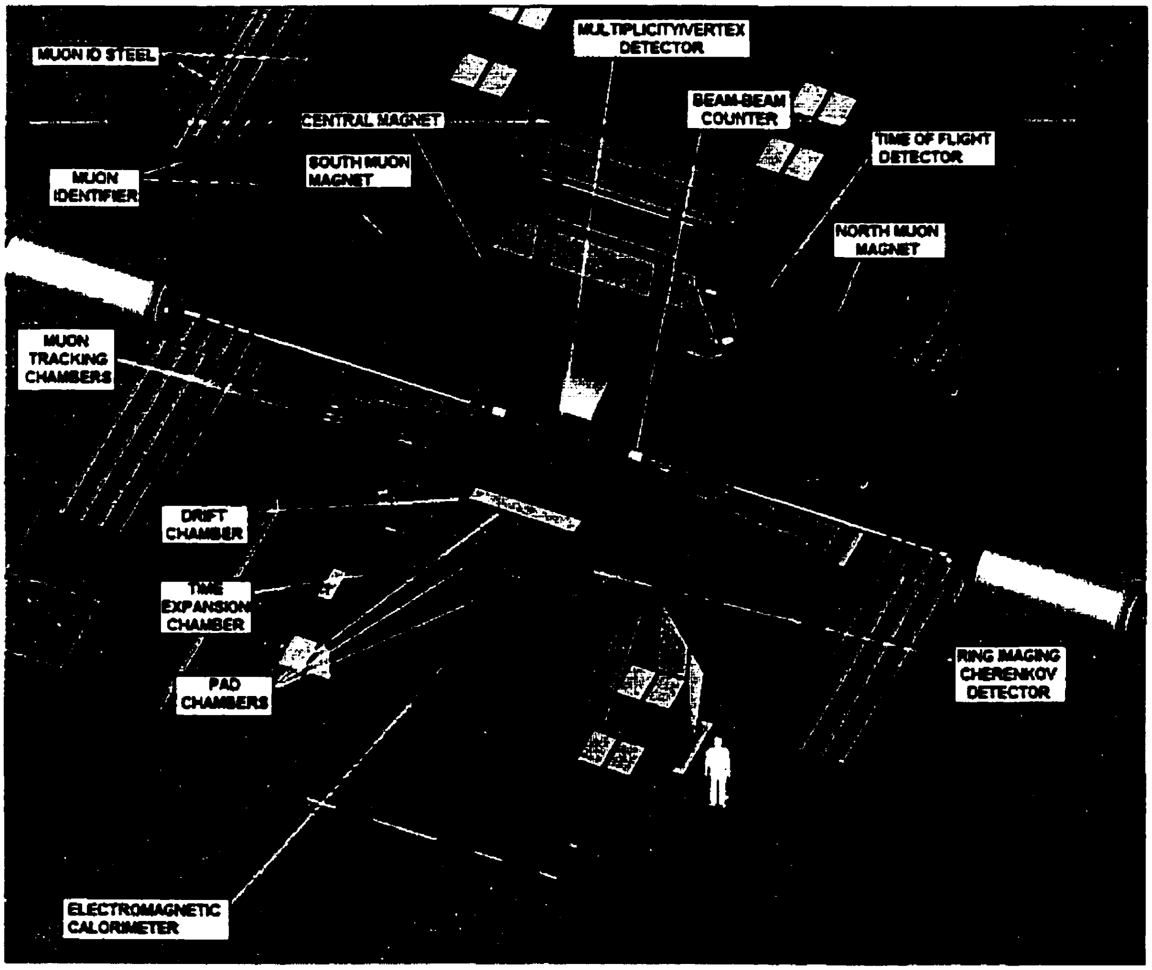

Figure 1.1: The PHENIX Detector. Overview.

range of particles and momenta. Time-of-flight (TOF) counters serve as a particle identification devices for hadrons and provide trigger capabilities. The ring-imaging Cherenkov detector (RICH) serves as one of the primary devices for the identification of electrons. Electromagnetic calorimeters (EM Cal) have two important roles: identification of electrons and photon measurements. Conventional drift chambers (DC) are used to provide high resolution p_T measurements and to participate, together with pad chambers (PC), in the pattern recognition by providing tracking information that is used to link tracks in the various PHENIX central detector subsystems. PC, DC together with time expansion chambers TEC constitute the central tracking system. TEC is also used to determine the particle species using dE/dx information. Global observable measurements, such us the total multiplicity, will be accomplished with multiplicity vertex detectors. A beam-beam counter (BB) provide the start timing and a fast estimate of the collision vertex position along the beam. A hadron blind Dalitz rejector is used to reduce the combinatorial background.

1.3 Pad Chambers

McGill University nuclear physics group joint the effort for the development, design and construction of a new type of multi-wire proportional chambers (MWPC) with pixel cathode pad readout called pad chambers. There are three layers of pad chambers in each arm of the PHENIX detector, PC1, PC2 and PC3 (see figure 1.2). First layer (PC1) consists of 8 planar sectors (the approximate dimensions of each sector in $x \times z$: 0.8 $m \times$ 3.2 m) each sector being a MWPC, is placed immediately behind the DC and in front of the RICH. Both PC2 and PC3 have 4 sectors (1.1 $m \times$ 5.0 m and 1.3 $m \times$ 6.0 m respectively) and will stay behind the RICH on the inside and outside of the TEC tracking detector, respectively.

The main function of PC is:

- To provide track information to reduce track matching ambiguities.

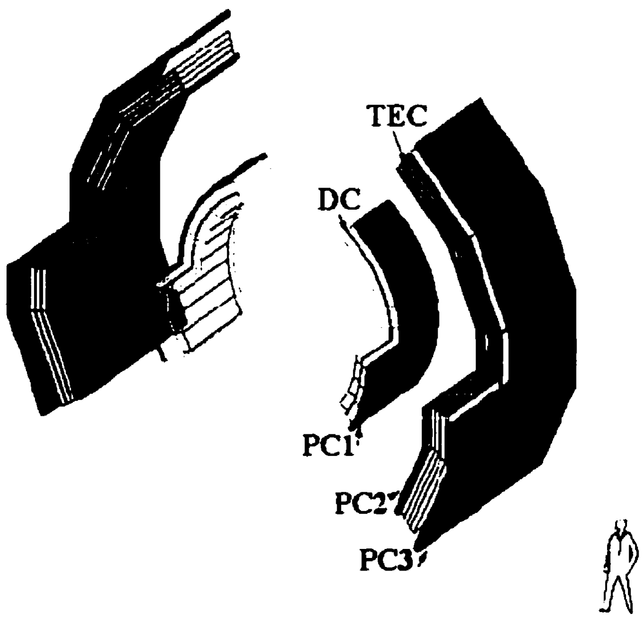

Figure 1.2: Overview of the PHENIX tracking system. The Pad Chambers (PC) are indicated by the shaded volume.

- To help separate neutral EM Cal showers from charged tracks.
- To provide azimuthal tracking information.
- To help veto the converted photons.

The expected position resolution is 4 mm in both directions for PC1 and 7 mm and 8 mm for PC2 and PC3 respectively. In order to minimize the background (like the photon conversion), the effective thickness should correspond to $\approx$ 0.5% of a radiation length for PC1, and no more than 1% for PC2 and PC3.

1.4 Purpose of the Present Thesis

McGill University has developed and tested several prototypes pad chambers for the central tracking system of the PHENIX detector. They are multi-wire proportional chambers with the cathode board segmented into small units called pixels, grouped in pads. Each pads has a digital readout system, and an interpolation method is used to determine the position of the particle. The main purpose of this thesis was the integration and test of a new digital readout electronics into the new prototype pad chamber PC1 - 1/4 scale (covers one-quarter of the planar surface covered by the final unit sector). Several relevant parameters of both readout cards operation and chamber operation were measured intending to test if they meet the PHENIX requirements. This thesis is divided in six chapters. After the presentation (second chapter) of the principles of operating in a MWPC and a short review of the methods of interpolation, the third chapter gives a detailed description of the operation of the present prototypes. The test of these prototypes, with cosmic rays and X-rays, are comprised in the fourth chapter. The fifth chapter shows simulation data and compares them with the experimental ones. Conclusions are presented in the sixth chapter.

Chapter 2

Principle of Operation of Multiwire Proportional Chambers (MWPC)

This chapter reviews the general principles of operation of MWPCs and exposes some of the particularities of the new pixel pad chamber.

2.1 General Considerations.

Since the introduction of the MWPC in 1968 it has been widely used in the detection of charged particles as well as photons. Its good positions resolution as well as practical reasons, such as the ease of construction and capability to realize a large active area, made MWPC one of the most popular tracking devices in experimental high energy physics.

A typical structure of a MWPC is illustrated in figure 2.1. It mainly consists of two cathode planes which confine a volume filled with ionizing gas and, between the cathode planes, an anode plane consisting of equidistant thin anode wires (several tens of microns in diameter). Field wires could be interceded between the anode wires in order to shape the field. The field wires are usually several times thicker than the anode wires. *The coordinate system presented in this figure will be used throughout*

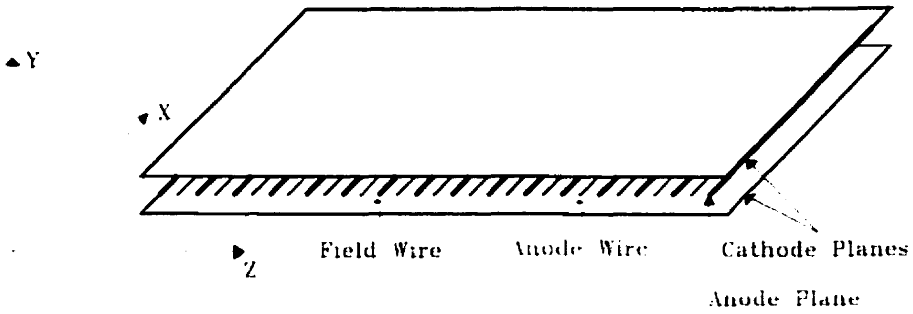

Figure 2.1: Typical structure of a MWPC.

this thesis.

When an energetic charged particle passes through a gas, it undergoes a series of inelastic Coulomb collisions with the electrons of the gas molecules. As a result electron-ion pairs are created along the trajectory. A high electric field will be formed around the anode wire when a positive high-voltage is applied to it. The fast drifting of the electrons toward the anode will ionize by collision other electrons and, if the electric field is sufficiently large, an avalanche will occur. The avalanche will be proportional to the number of primary electron-ion pairs created. The determination of the position of this avalanche gives information about the position of the incident particle.

2.2 Energy Loss Mechanism

The energy loss mechanism is different for charged particles and for photons. A charged particle passing through a gas loses its energy by the excitations and ionizations of gas molecules as a result of its inelastic collisions with the electrons of gas molecules. There are two types of ionizations, primary and secondary [16].

In primary ionizations, one or more electrons are ejected from an atom (A) encountered by a fast particle, say a π meson:

$$\pi A \rightarrow \pi A^+ e^-,\ \pi A^{++} e^- e^-$$

Most of the charge along a track is however from secondary ionizations where the electrons are ejected from atoms not encountered by the fast particle. This happens either in collisions of ionization electrons with atoms or through atomic intermediate excited states A^*:

$$\pi A \rightarrow \pi A^* \quad or \quad e^- A \rightarrow e^- A^*$$
$$\Rightarrow A^* B \rightarrow A B^+ e^-$$

The ionization potential of B have to be lower than excitation energy of A. A^* is often the metastable state of a noble gas and B is one of the molecular additives (quenchers) that are required for the stability of chamber operation.

The energy loss is dependent on the distance traveled by the particle in the gas, particle velocity ($\beta = v/c$), particle charge (z), and some gas parameters: atomic number, mass number and density (Z and A_0, ρ) and effective ionization potential averaged over all electrons ($I = I_0\ Z, I_0 \approx 10eV$ for $Z > 30$). Quantitatively the stopping power of a charged heavy particle is given by the Bethe-Bloch formula [17]:

$$\frac{dE}{dx} = -2K\frac{Z}{A_0}\frac{\rho}{\beta^2}[ln(\frac{2m_e v^2}{I(1-\beta^2)}) - \beta^2], \qquad K = \frac{2\pi N_0 z^2 e^4}{m_e c^2} \tag{2.1}$$

where m_e is the electron mass and N_0 is Avogadro's number. It is interesting to observe that dE/dx is independent of the particle mass M. It varies as $1/v^2$ at non-relativistic velocities, reaches a minimum for $E \approx 3\ Mc^2$, and increases logarithmically at high energy with the relativistic rise $\gamma = \frac{1}{\sqrt{1-\beta^2}}$. As a result, all high energy charged heavy particles tend to have more or less the same stopping power value, and they are called the minimum ionizing particles (MIP).

Because of the fluctuations in the energy loss process, the energy loss presents a broad distribution. A classical description of the energy loss distribution in a thin absorber (in which the energy loss is negligible compared with the total energy of the particle) is due to Landau and predicts a distribution that can be parameterized as::

$$f(\lambda) = \frac{1}{2\pi} e^{-\frac{1}{2}(\lambda + e^{-\lambda})}, \tag{2.2}$$

where λ represents the normalized deviation from the most probable energy loss ΔE_{MP}:

$$\lambda = \frac{\Delta E - \Delta E_{MP}}{\xi}, \qquad \xi = K \frac{Z}{A} \frac{\rho x}{\beta^2}$$

where ρ is the density of the absorber and x is the thickness.

Interaction between low energy photons and gas molecules is mainly by photoelectric effect. It is a single localized event. Let's consider the photon energy E_γ. If the photon is absorbed by a molecule with a shell energy E_i, the correspondent photoelectron will be freed with the kinetic energy $T = E_\gamma - E_i$. The excited ionized molecule will return in its ground state mainly through following processes:

Fluorescence The shell vacancy is filled with an outer shell electron by emitting a photon of energy $E_i - E_j$.

Auger Effect It consist in an internal reordering involving several outer shell electrons. The outcome is the filling of the inner shell vacancy by an outer shell electron (with binding energy E_j) and emission of an outer shell electron with energy $E_i - 2E_j$.

If the fluorescent photon escapes from the detector gas volume, a deficit in the deposited energy appears (the escape peak in the energy spectrum).

The data presented in figure 2.2 are collected during the cosmic ray and X-ray tests with our detector. A fit of the experimental data with a Landau function is presented as a solid line in the left-hand side. The right-hand side shows the anode charge spectrum obtained with our detector using a ^{55}Fe source emitting X-rays of energy 5.9 KeV. The spectrum is characterized by a relatively narrow peak.

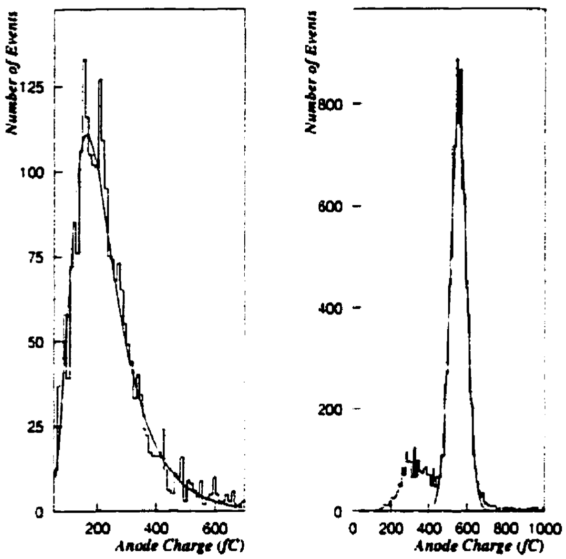

Figure 2.2: Typical anode charge spectrum measured in our test chamber: (**Left**) with cosmic rays and (**Right**) with ^{55}Fe X-ray source.

2.3 Amplification of Ionization. Anode Avalanche

Among all the amplifiers of the feeble energy deposited by a particle on its passage through the matter, the proportional wire is a particularly simple and well-known example. The primary created electrons drift toward the anode wire along the electric field lines. They travel in an increasing electric field, which, in the vicinity of the anode wire at radius r, is given by:

$$E = \frac{\lambda}{2\pi\epsilon_0}\frac{1}{r} \tag{2.3}$$

where λ is the linear charge density on the anode wire. It depends on the specific geometry of the detector and the anode voltage applied.

Figure 2.3 shows the electric field distribution, inside a typical MWPC, generated using GARFIELD [18] simulation software. If the electric field is strong enough the electrons could pick up sufficient energy to induce further ionizations between the

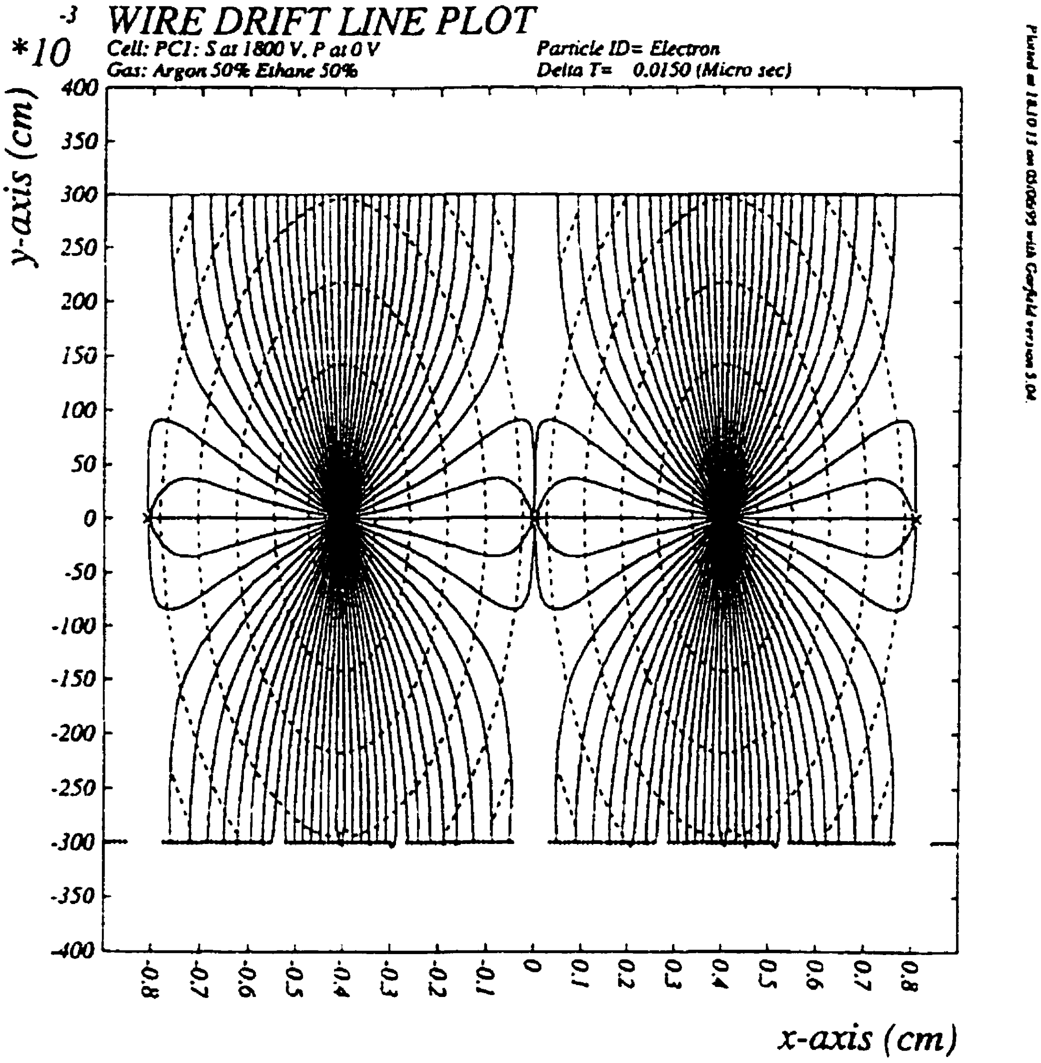

Figure 2.3: Calculated electric field lines (solid lines) and equi-time lines (dashed lines) in PC1 obtained with the code GARFIELD. The drift time between two consecutive equi-time lines is 15 ns. This calculation result is for an anode voltage of 1800V and a gas mixture of 50% Ar – 50% Eth. The "$y = 0$" plane is the anode plane. The wires surrounded by a high density (low density) of electric field lines are the anode (field) wires. The "$y = -300 * 10^{-3}$ cm" and "$y = +300 * 10^{-3}$ cm" planes represent the two cathode planes.

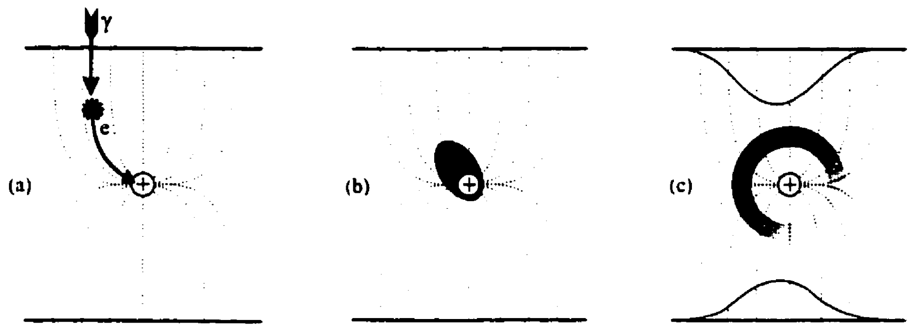

Figure 2.4: Illustration of the avalanche process. (a) Creation of an electron-ion pair. (b) Asymmetric avalanche. (c) Drift of the positive ions. The charge induced on the cathode plane is asymmetric as well.

collisions with the gas molecules. In this case other electrons are created and the avalanche starts. At normal gas density the mean free path between two collisions is of the order of microns. In this conditions the magnitude of the field that starts the avalanche is about 10^4 V/cm. Consequently the anode wire has to be about tens of microns thin. for 1-2 kV voltage applied on the anode [19]. The avalanche does not always surround uniformly the wire but develop preferentially on the approach side of the primary electrons as schematically illustrated in figure 2.4 (for calculations on the angular distribution see [20]). The whole process develops in the drift direction over as many free paths as multiplying generations exist. typically $50 - 100$ μm.

The positive ions will drift toward the cathode plane. but their drift is about thousand times slower compared with electrons. In avalanches with a large number of electron-ion pairs. the presence of the positive ions surrounding the anode wire can form a positive charged "cloud". It effectively reduces the electric field strength. This process is known as the space charge effect and could reduce the amplification factor.

2.4 Induced Charge on Electrodes

The moving charge between the electrodes give rise to electrical signals. The readout electronics is connected to either the anode or one of the cathode planes in order to detect the induced charge. The time evolution of the electrical signals will be related to the charge drifting and a spatial distribution (determined by the geometry of the detector).

2.4.1 Time Dependence of the Signal

To discuss the time dependence of the signal, it is easier to consider our detector having a cylindrical shape with r_a and r_c the radii of the anode and cathode respectively. If V_a is the anode voltage and the cathode voltage $V_c = 0$, then the electric field at distance r from the center is:

$$E(r) = \frac{1}{\ln(r_c/r_a)} \frac{V_a}{r} . \tag{2.4}$$

and the electrical potential:

$$V(r) = V(a) \left[1 - \frac{\ln(r/r_a)}{\ln(r_c/r_a)} \right] . \tag{2.5}$$

Let's assume that the avalanche process creates the charge $+q_0$ (positive ions) and $-q_0$ (electrons). As stated before most of the multiplication process take place within few mean free paths from the anode surface. It is then reasonable to consider that the process take place near the anode surface. The signal current will then be given by [21]:

$$i_c = i_a = \frac{q_0}{t_0} \frac{1}{2\ln(r_c/r_a)} \frac{1}{1 + t/t_0} \tag{2.6}$$

where,

$$t_0 = \frac{r_a}{2\mu E_a}$$
$$E_a = \frac{V_a}{r_a \ln(r_c/r_a)}$$

and μ is the positive ion mobility, independent of the electric field.

This equation holds only for two electrode system. For multiple electrode detectors the charge will be distributed among electrodes. In our case, due to the symmetry, the charge will be evenly distributed between the two cathodes. For an arbitrary electrode configuration other calculations of the induced charge were proposed (such as the Weighting-Field concept developed by Radeka [22]).

2.4.2 Spatial Distribution of the Cathode Charge

Because of the simple geometry of our detector, a convenient way to calculate the induced charge distribution on the cathode is the image method. In this method we assume that the charge is point-like (Q_A) and is situated midway between the two cathode planes. The image charge is an infinite series of point charges situated along the line passing through initial point and normal to the plane [23]:

$$\rho(x,z) = \frac{-Q_A}{2\pi}\sum_{n=0}^{\infty}(-1)^n \frac{(2n+1)h}{[(2n+1)^2h^2 + x^2 + z^2]^{3/2}} \tag{2.7}$$

The charge distribution along one dimension can be derived by integrating equation 2.7 over the second dimension:

$$\rho(x) = \int_{-\infty}^{+\infty} \rho(x,z)dz$$

and the result will be:

$$\rho(x) = \frac{-Q_A}{4h} sech \frac{\pi x}{2h} \tag{2.8}$$

A three parameter empirical formula was developed by Gatti et al. [24] for the induced charge distribution along the anode direction. Mathieson [25, 26] calculated the one dimensional distribution both along the wires and perpendicular to them. It was found that the difference between the induced charge along the anode wire is, for all practical purposes, negligible compared with the distribution across the wires. They also developed a single parameter empirical expression, based on the Gatti formula [27, 28], as follow:

$$\rho(\lambda) = Q_A \; K_1 \frac{1 - tanh^2(K_2\lambda)}{1 + K_3 \; tanh^2(K_2\lambda)} \tag{2.9}$$

where:

$$\lambda = \frac{x}{h} \quad (normalized\ coordinate)$$
$$K_1 = \frac{K_2\sqrt{K_3}}{4\arctan\sqrt{K_3}}, \quad K_2 = \frac{\pi}{2}\left(1 - \frac{1}{2}\sqrt{K_3}\right)$$

A typical shape of this distribution can be seen in figure 2.5. The absolute height and width of the distribution is proportional to the magnitude of the avalanche and chamber dimensions respectively.

2.5 Position Determination. Methods of Interpolation in MWPC

The charge collected by the anode wire could be readout using low noise front end electronics. A detailed description of the operation of such a device will be presented in the next chapter. The distribution of the charge collected by the wires give the coordinate of the incident particle in the direction perpendicular to the wires (x). Therefore, a single plane of MWPC can give position information only in the x direction. Another plane of MWPC, with anode wires running orthogonal to those of

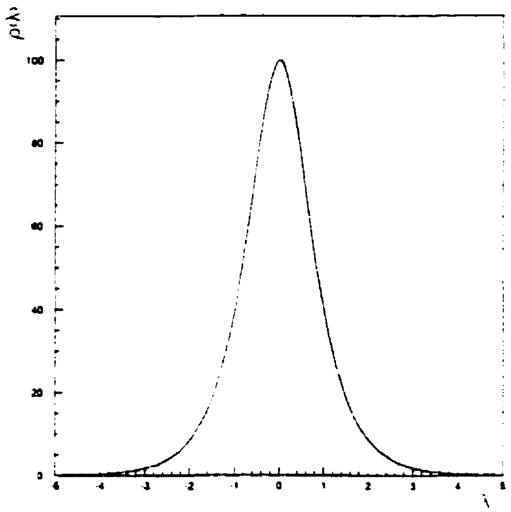

Figure 2.5: Typical shape of the induced charge distribution on the cathode.

the first, is needed to give information in the z direction (parallel to the wires of the first MWPC). However, this will only work for single particle events. For two particles hitting simultaneously the chamber, another two "ghosts" (false particles) will appear(see fig. 2.6). Three layers could resolve two particles but they cannot resolve three. For higher multiplicity a higher number of MWPC is needed and consequently a larger number of readout channels. In experiments at relativistic heavy ion colliders the detectors should be able to provide accurate tracking for multiplicities of the order of 10^3 p/sr. It is obvious that this method cannot fulfill the requirements of such experiments.

Several methods of "getting around" this problem were proposed. A comprehensive review of these methods can be found in reference [29]. We will give here only an overview of these principles with emphasis more on the principles of operation of the present prototype.

The basic idea is to use multiple readout channels for a single wire. Another possibility is to use a segmented cathode plane and to readout the image charge collected on individual cathode segments (pads). The position resolution is given

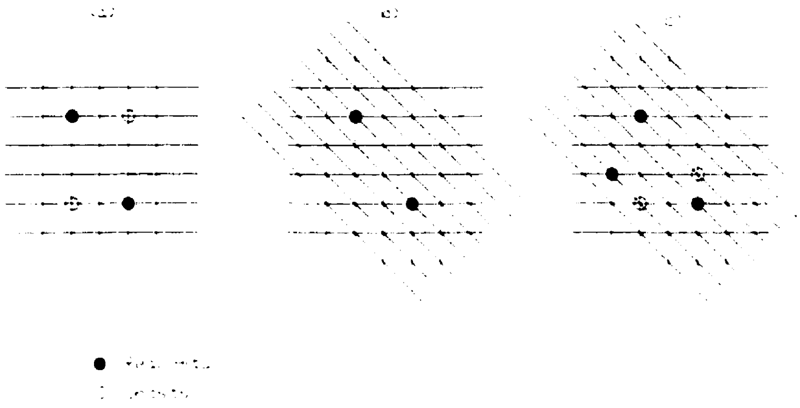

Figure 2.6: Ambiguity in the position determination. By "•" we show the real hits and "o" indicate ghosts. Two layers cannot resolve two hits (a). Three layers resolve two (b) but cannot resolve three hits (c).

by the anode wire spacing ($\sigma = s/\sqrt{12}$) [30], in one direction, and the readout spacing in the other. An interpolating method uses the signal from several readouts in order to provide finer resolution than the readout spacing. There are three main types of interpolating methods: resistive charge division [31, 32], capacitive charge division [33, 34] and geometrical charge division [35, 36, 37, 38, 39]. Here is a brief description of each of these methods:

Resistive Charge Division: A detector using resistive charge division has a finite resistance in its readout electrodes. The charge collected by the readout is inversely proportional with the resistance between the initial signal and readout node. Several readout systems collect the charge from one electrode and use this principle to determine the avalanche position.

Figure 2.7 (top) shows a schematic view of a MWPC functioning accordingly to this principle and using the charge collected by only the anode wire. Figure 2.7 (bottom) presents a MWPC based on this principle as well, but using the cathode charge information to determine the avalanche position. The cathode plane is divided into strips interconnected by resistors. At regular intervals the strips are connected to readout systems (charge sensitive preamplifiers in

Anode Wire Charge Division

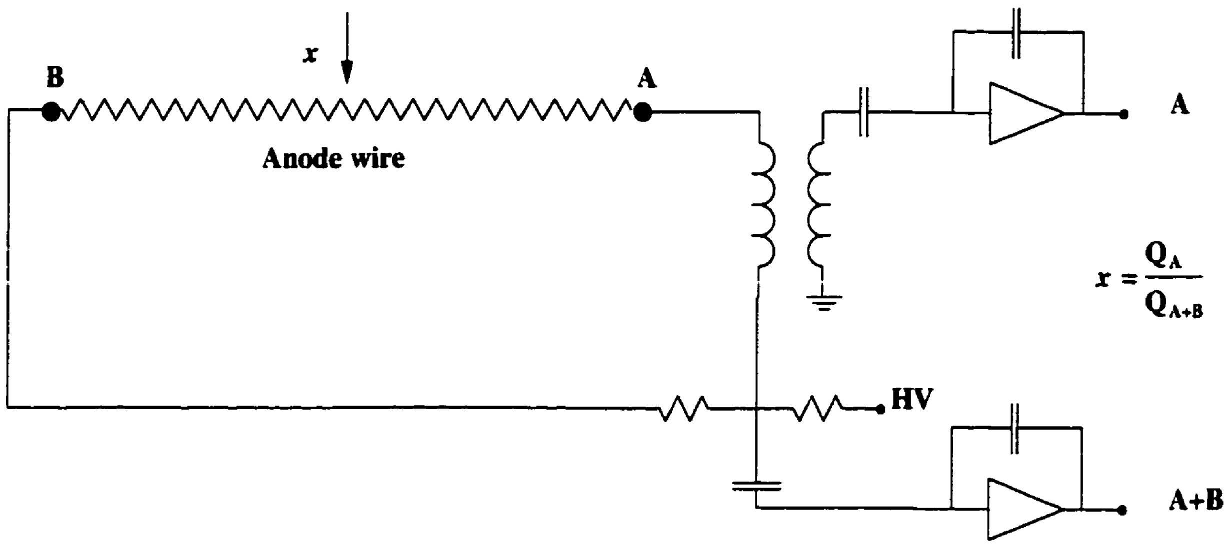

Resistively Coupled Cathode Strips

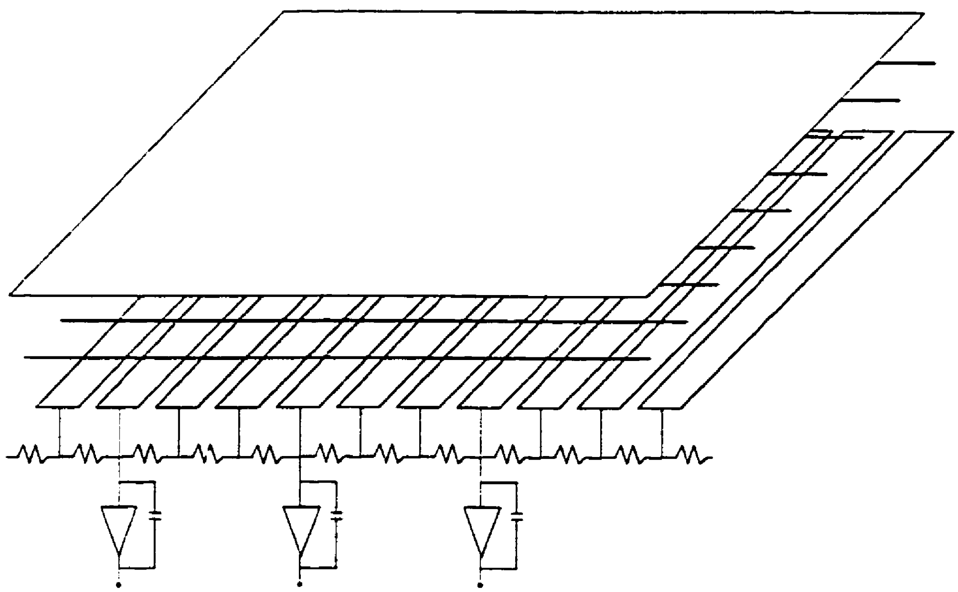

Figure 2.7: MWPC with Resistive Charge Division. **Top**: anode wires charge division. **Bottom**: resistively coupled cathode strips.

this case). The centroid of the induced cathode charge (normal to the strip direction) can be calculated by using signals from only few readout channels.

Capacitive Charge Division: The principle is very similar to the resistive charge division, but utilizes the intrinsic capacitive coupling between cathode strips to generate a charge division.

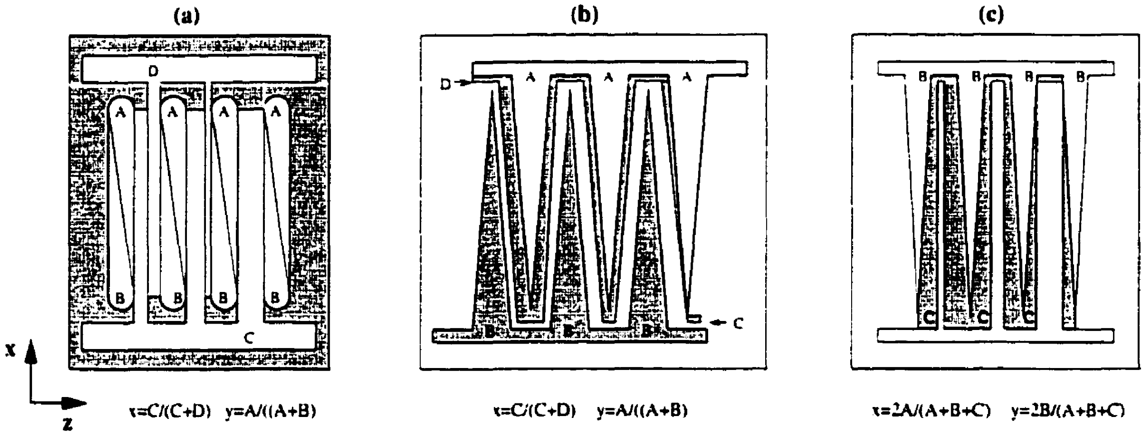

Figure 2.8: Wedge and strip geometrical cathode division. This figure is reproduced from [21].

Geometrical Charge Division: As previously shown, the induced charge on the cathode plane from an avalanche is localized in an area with a specific geometrical distribution. Another type of interpolating method is accomplished by using specially shaped electrodes to sample the image charge. Such an interpolating scheme, the "wedge and strip" geometry proposed by Anger [40], is shown in figure 2.8(a). Electrodes A and B are wedge shaped, with the width varying along x direction. Along the z direction the width of the cathode strips C and D varies in opposite directions: one increase while the other decrease. The charge collected by the cathode electrodes varies with the relative position from avalanche. Therefore the avalanche position could be determined with good accuracy. The interpolation formulas are written below the figure. Figures 2.8 (b)&(c) show two variations of the wedge and strip cathode pattern.

In order to improve resolution and handle higher multiplicities, a finer segmentation of the cathode plane into smaller cathode segments (called pads) was later proposed. The pads of a specific geometrical shape are used to sample the charge induced on the cathode. The relative value of the induced charges on the pads determines the avalanche location. Each pad is directly connected to a charge sensitive amplifier, connected itself to an analog readout system to determine the amount of charge collected. Various patterns of cathode pads were proposed [41, 42].

Following the evolution of many geometrical charge division methods, the chevron pad was developed and was proposed as an alternative of the present prototypes for the PHENIX project. The heavy-ions group from McGill University is working for the development of the pad chambers to be included in the tracking system of the PHENIX detector. During this research and development work prototypes of chevron pad chambers were built [43]. The shape of the chevron pad and its position related to the anode wire is shown in figure 2.9. The chevron pads are arranged in a column lying beneath the anode wires. In

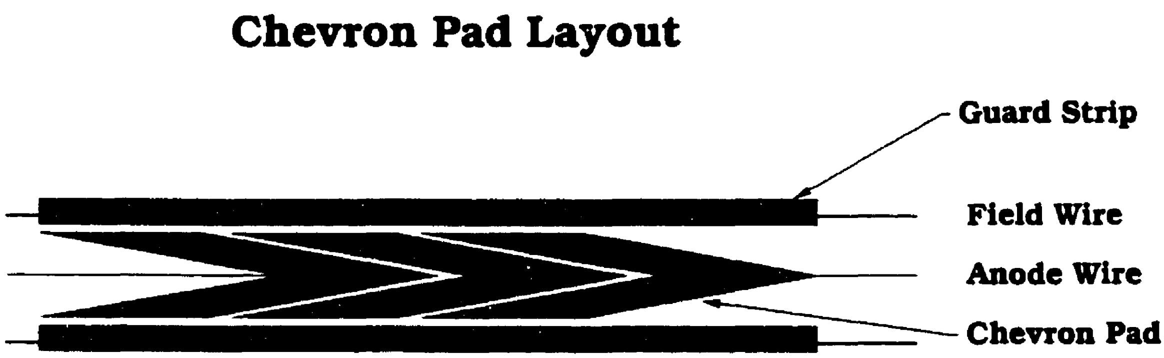

Figure 2.9: Chevron pad pattern.

such configuration the induced charge on the cathode is shared by at least two neighboring chevron pads. The position of the avalanche is, to the first order, proportional to the amount of charge deposited on each pad. For a given position resolution such design allows a significantly larger readout node spacing than those using rectangular pads, and thus results in a reduced number of readout channels. A position resolution of the order of 1-1.5% of the readout spacing was achieved [43].

Although they offer a good position resolution, the chevron dimensions have to be small to successfully deal with high multiplicities like those in the PHENIX experiment. This will increase the number of readout channels and the cost of such a detector [44].

2.6 Method of Interpolation using Pixel Pad Cathode Readout

Experiments like those being conducted with high-energy heavy-ion beams have shown the importance of developing pad chambers capable of handling events with high multiplicity. The idea of a highly segmented cathode plane divided into pixel-like square pads was introduced [45, 46]. A schematic view of such chamber is shown in figure 2.10. A charged particle traversing the detector leaves an induced charge on a few localized pads. A centroid-finding readout system allows position determination to a small fraction of the basic cell size.

In order to handle events with high-multiplicity like those expected from future high-luminosity colliders such as RHIC, and also to obtain the desired position resolution, we have to substantially increase the number of pixel-pads (and, by the same quantity, the number of readout channels). The squared pixels (as well as all the other designs presented above) present another disadvantage. A noisy or dead channel means a dead region of the detector.

In order to solve some of these problems a new type of pad cathode division was designed (see fig. 2.11) and proposed for the pad chambers of the PHENIX detector. The cell is the basic unit of the reconstruction process. Every cell is formed by three

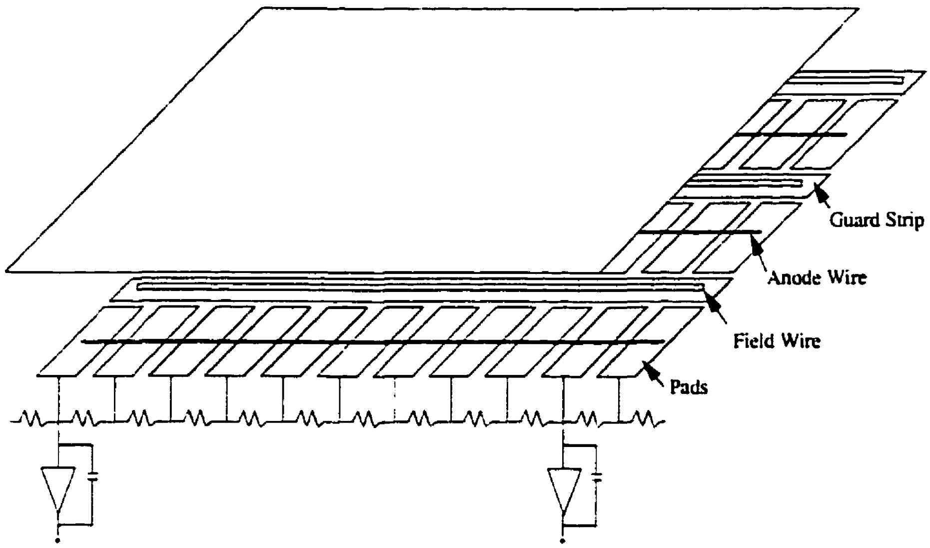

Figure 2.10: Example of MWPC having cathode with pixel pad pattern.

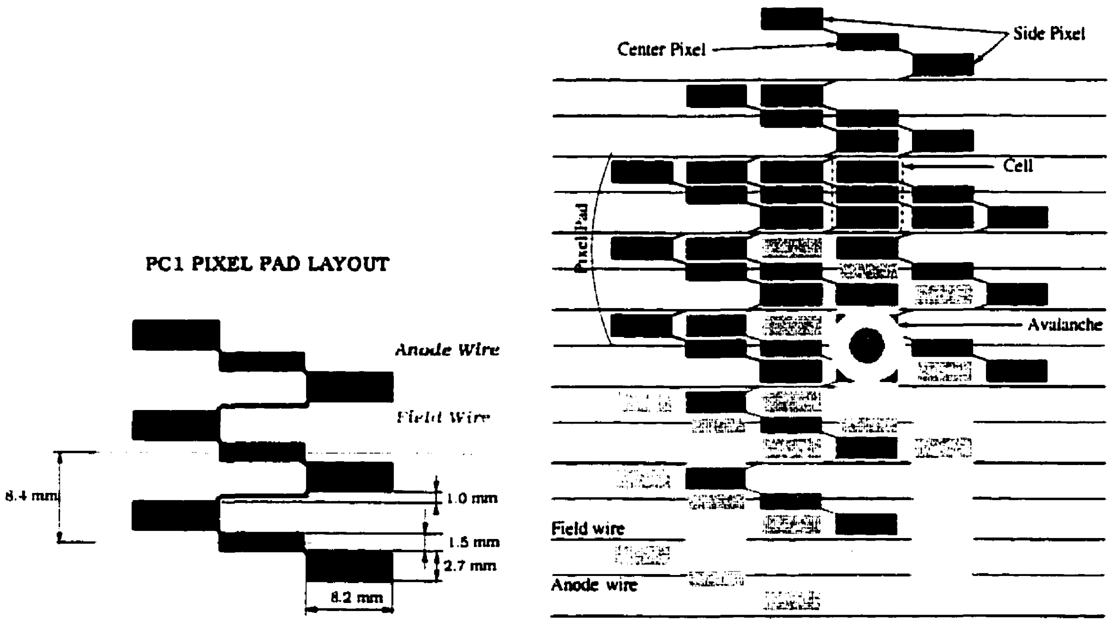

Figure 2.11: The new pixel pad cathode pattern.

rectangular pixels, as shown in the right-hand side of figure 2.11. As one could see in this picture, one pixel is centered on the anode wire and is separated by the two other side pixels by a small insulating spacing. Nine pixels are linked together forming a pixel pad (or simply "pad"), in such a way that any cell is formed by three pixels correspondent to a unique combination of three pads. Such a pad is individually represented in the left-hand side of the same figure. Each pad has its own digital readout. We call "channel" the output of this readout, therefore, we will say that a pad is fired if we have signal in the correspondent readout channel. We say that a cell is fired if all three pads, contributing with one pixel to that cell, are fired. A resolution less than half of the cell dimension is expected.

This specific design of the cathode plane offers two main advantages. The design of the cell formed by three pixels gives us the possibility to cope with eventually dead channels. In the eventuality of a dead channel we still can identify the presence of a signal in the cell region by detecting the charge induced on the other two pixels. In this special case we can accept a cell to be considered fired if only two contributing pads are fired. By linking nine pixels in order to form a pad, we reduce the number of readout channels by a factor of almost three if it is compared with a one-pixel cell pattern with the same dimension. The reduction factor is nine if it is compared with a three-pixel cell pattern.

The new prototypes pad chambers with pixel pad cathode readout designed, built and tested at McGill will be described in the next chapters.

Chapter 3

The New Prototype of Pixel Pad Chamber. Detector Construction and Operation.

Three prototypes pad chambers with pixel pad cathode and digital readout have been developed and built at McGill University: PC1 (one-quarter the size of the final unit sector). PC3 (1/8 scale) and PC1 (full scale). PC1 (1/4 scale) was used for the tests described in the present thesis. The figure 3.1 shows an overview of the PC1 (1/4 scale) prototype and the experimental setup used during the tests.

3.1 Mechanical Structure and Chamber Assembly

A top and cross section view of the PC1 (1/4 scale) prototype chamber is given in figure 3.2. The basic structure of the chamber consists of two cathode planes and a FR4 fiberglass frame confining the gas volume. In the middle there is an anode wire plane where the anode and field wires are equidistantly aligned. Two honeycomb panels of different thickness are used for the structure of the two cathode planes.

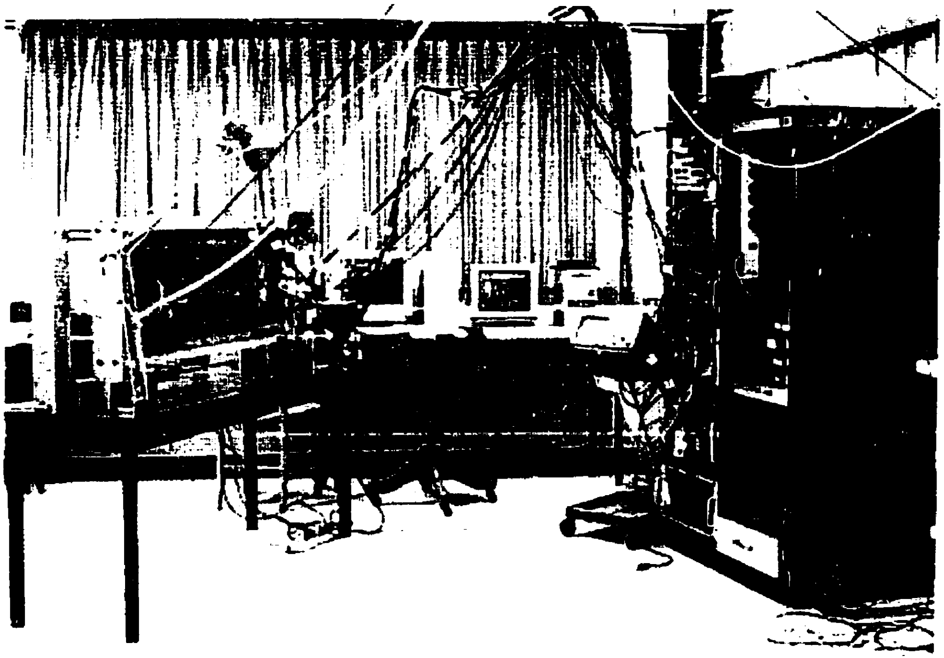

Figure 3.1: PC-1 (1/4 scale) prototype and the test setup.

- The motherboard is glued on one side of the first panel (made of HEXEL honeycomb, one inch thick). The motherboard is made of a thin fiberglass sheet and has imprinted circuit lines so that the detector electronics can be mounted on it (see fig. 3.2, bottom). The pixel cathode board is glued on the other side. The pixel-board is made of 250 μm FR4 fiberglass. On one side, pixel-pads made of 8.6 μm thick copper are etched. On the other side, copper traces are connecting the pixels with surface-mounting connectors. Plated-through holes connects the pixels-pads from one side with the traces which lead to the connectors (located on the other side). After a careful examination of the contact of all plated-through holes, they were covered with conducting glue to prevent gas leakage through the pixel board. The connection between the connectors glued on the pixel board and those glued on the motherboard is done using specially made high pitch kepton cables. These cables pass through cutouts made in the honeycomb panel.

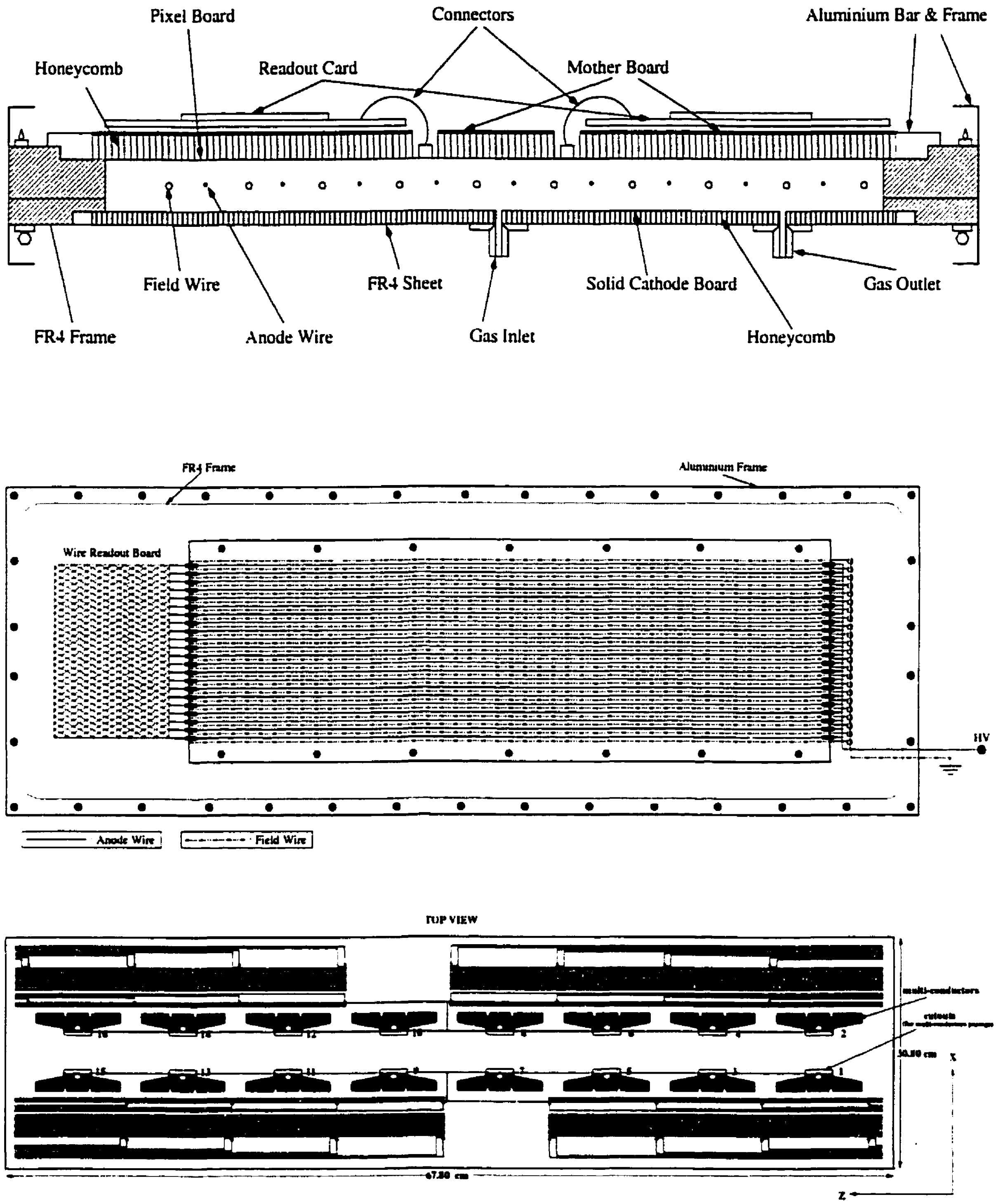

Figure 3.2: PC-1 (1/4 scale) schematic view. **Top:** cross section view. **Middle:** top view. **Bottom:** motherboard design and readout card places and numbering scheme.

- On the second panel (a quarter inch thick) a FR4 fiberglass (250 μm thick) and a copper board (8.6 μm thick) are glued to the honeycomb panel to make a "sandwich" panel (the solid cathode panel). Two cutouts are made in the solid cathode panel for fixing the gas inlet and outlet .

Two high-precision pitch bars were glued at the edge of the pixel board to guide the anode and field wires, which were precisely aligned with respect to the pixel columns. Wires passing through these pitch bars were soldered on terminal boards glued at the edge of the pixel cathode board. Tungsten rhenium wires (ϕ = 25 μm, plated with gold) were used as anode wires and beryllium-copper wires (ϕ = 125 μm) were used as field wires.

The two honeycomb boards are mounted on a FR4 fiberglass frame, so closing the gas volume. The whole assembly was ascertained to be dust free before the two FR4 frames were closed. The assembly process took place in a "clean room" with class 10000 air filters. For convenience, the detector was mounted on an aluminum frame. The mounting was performed on a high precision flat granite table. Finally the readout cards (ROCs) were soldered on the motherboard. The bottom of figure 3.2 shows the motherboard design and the numbering of the places where the ROCs are soldered. The fabrication procedures for the other prototypes were similar.

Table 3.1 summarize the PC1 quarter-scale prototype parameters.

3.2 Cathode Board Design

The pixel cathode board was made of a 250 μm thick FR4 fiberglass sheet with printed circuit on both sides. The copper thickness on each side is 8.6 μm. A specific pattern of the cathode board has been designed.

Figure 3.3 presents the basic unit of the cathode board pad structure. It contains 48 pad-channels connected to one readout card. The entire cathode board is obtained by duplication of this basic unit. The edge pads (channels) corresponding to one card

Table 3.1: Prototype PC1 (1/4 scale) Parameters

Number of Anode Wires	22
Number of Field Wires	23
Number of Readout Cards	16
Number of Readout Channels	768
Anode Wire Diameter (μm)	25
Field Wire Diameter (μm)	125
Anode to Anode Wire Spacing (mm)	8.4
Anode to Field Wire Spacing (mm)	4.2
Anode Wire to Cathode Spacing (mm)	3.0
Active Cathode Plane Width (mm)	188.3
Active Cathode Plane Length (mm)	781.65

intercede with the channels of another card in order to form a cell. At the edge of the board. those pixel pads staggered outside the center square of 10 x 10 complete cells were cut. Those pixels corresponding to incomplete pads were specially connected together according to their original connection pattern. The middle of one row of cells in the z direction corresponds to an anode wire level. while the small interspace between two rows of cells corresponds to a field wire level. The dimensions of the three pixels in each cell were chosen so that a centrally located avalanche around one anode wire will produce roughly the same amount of charge on the central and side pixels. The size of the cells is chosen so that it will be possible to attain the required resolution: 4 mm, 7 mm, 8 mm for PC1, PC2 and PC3 respectively. The relevant dimensions for the cathode board of the PC1 prototype used in this tests are summarized in table 3.2.

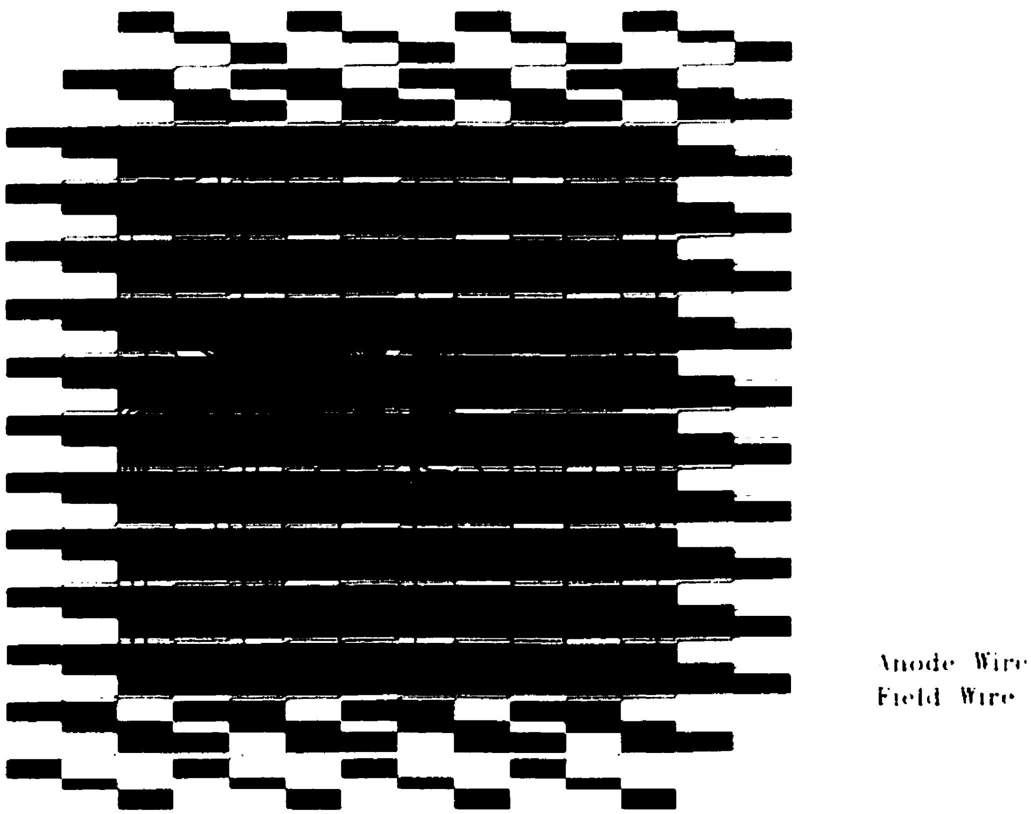

Figure 3.3: Basic unit of the cathode board.

3.3 Detector Electronics

3.3.1 Pad's Charge Readout.

A schematic view of the pads readout is shown in figure 3.4. A new digital front end electronics with highly integrated CMOS chips was built and assembled in specially designed readout card (ROC), mounted directly on the motherboard. The ROCs were designed, produced and tested by a joint collaboration with Lund University and Oak Ridge National Laboratory. Charge sensitive preamplifiers, shapers

Table 3.2: Cathode Board Parameters for PC1 (1/4 scale)

Pixel Length (*mm*)	8.2
Side Pixel Width (*mm*)	2.7
Center pixel Width (*mm*)	1.5
Adjacent Pixel Spacing (*mm*)	0.25
Cell spacing Between Pixel Columns (*mm*)	1.0
Pixel Corner Cut (*mm*)	0.2
Pixel Interconnection Width (*mm*)	0.2
Plated-through Hole Diameter (*mm*)	0.3

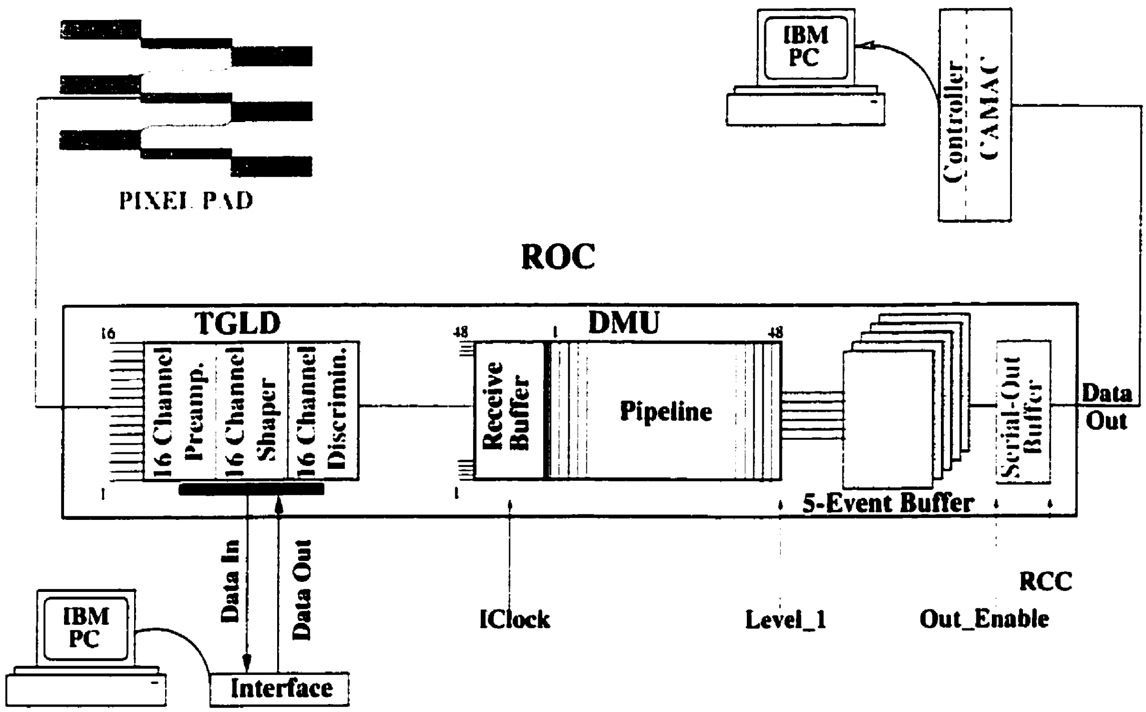

Figure 3.4: Pad readout logic diagram.

and discriminators are built inside specially designed chips called TGLD. Three 16-channels TGLDs, a digital memory unit (DMU) and two LTC489 receiver chips (for the serial communication with TGLDs and DMU), are mounted on the readout card (ROC) using chip-on-board (COB) technology (see figure 3.5).

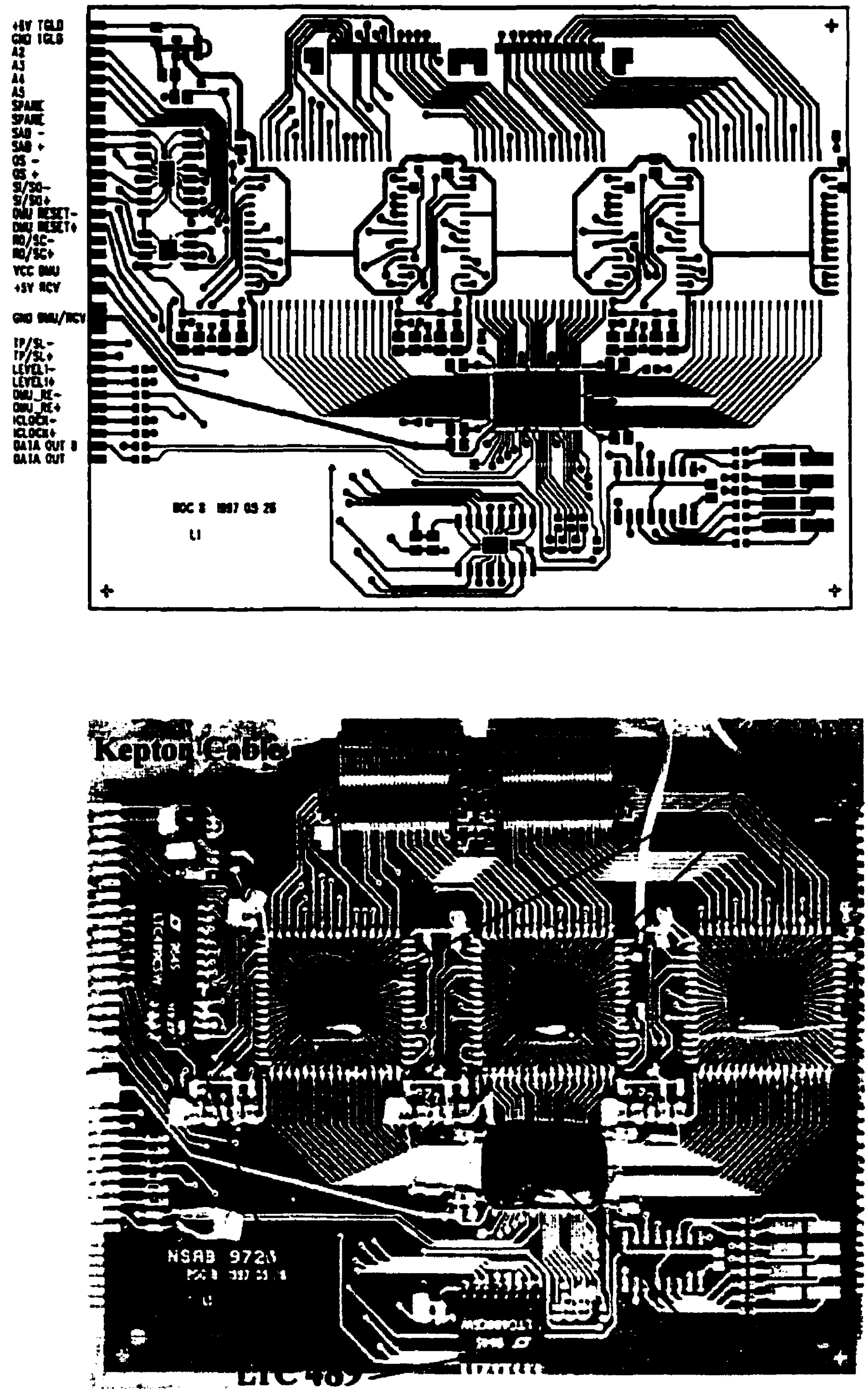

Figure 3.5: **Top:** ROC signal traces and the connections at the left edge which are soldered to the motherboard. **Bottom:** ROC picture.

TGLD chips

The amount of charge collected by the pads is very small (a few fC) and thus require the use of low noise front end electronics. The first step in the amplification process is the preamplifier/shaper multiplexer (MUX, 16 channels) which converts the input charge to a voltage output. The output of the system can be attenuated, in steps, by a factor of three up to a maximum factor of 27. Figure 3.6 shows the linearity of the preamplifier and shaper (multiplexer) and the saturation point for large input charges. The nominal gain is 10 mV per fC input charge. The signal is then

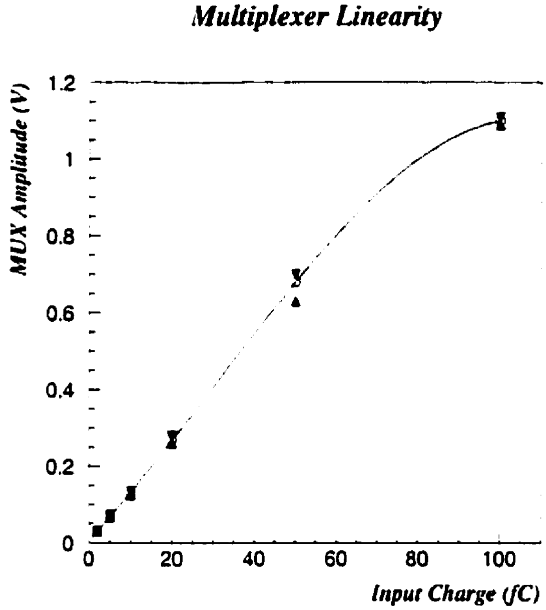

Figure 3.6: Multiplexer linearity and gain expressed in mV/fC for three channels of one chip with the nominal gain $10mV/fC$.

digitized by a 16-channel discriminator with a threshold programmable from 0.4 to 6 fC. This effective range is expanded by the adjustable attenuation of the shaper output. The discriminator produces pulses of standard height but variable width. The width is determined by the duration of the input signal above the threshold level. Figure 3.7 shows a typical output from the discriminator.

The multiplexer and discriminator are built inside a single 16-channel chip called

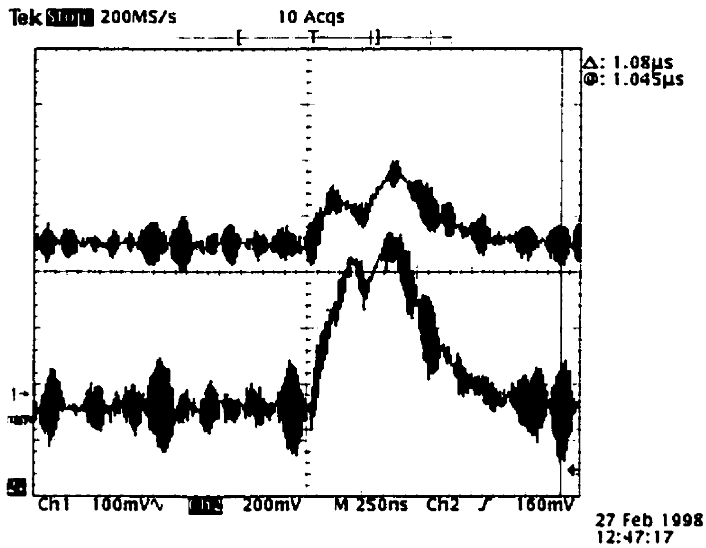

Figure 3.7: Typical discriminator output. Two channels fired simultaneously. The noise interfering with the output signal is partly due to the RFM pick-up noise of the oscilloscope's probe.

TGLD. The digital data from 3 TGLDs is then fed into a 48-channel digital memory unit (DMU), a sort of pipeline and event buffer.

Digital Memory Unit

The DMU serve the following purposes:

- Provide a temporary storage of the data until a trigger decision is made. The width of the memory is 48 data bits (one for each input channel of the 3 TGLD's). The depth of the memory is programmable up to 48 clock-cycles. In our experiments 40 were used.

- Provide a storage of the accepted events until the data readout is completed. It has a five events buffer, each of 48 data bits width.

The 48 parallel input signals (ID00-ID47) are driven from the TGLD's discriminator into the receiver buffer of the DMU. The receiver buffer has a latching mechanism which ensure that any input signal of length more than 5 ns will be fed into the delay memory on the next rising edge of the clock (ICLOCK). The nominal signal width of the discriminator output is 500 $ns - 1$ μs. The ICLOCK signal used had a frequency of 8 MHz (i.e. 125 ns period), so more than 1 timeslice is filled for an event. The data are then fed into a delay memory which is a sort of pipeline. The length of the pipeline is programmable between 0 and 48 clock-cycles. In our tests it was adjusted to 40.

The arrival of a LEVEL 1 signal starts the transfer of data from the delay memory to one of the event registers. A transfer could involve anything from one (corresponding to the LEVEL 1 signal) to several subsequent timeslices. The number of the slices to transfer is called the EVENT LENGTH and is programmable from 1 to 8. The event register is filled with the result of a bitwise **"or"** between the transfered slices. In other words: a bit in the event register shall be set if this bit was set in any of the transferred slices. In our experiments a logic "or" between 3 timeslices has been chosen. Data in a timeslice, not associated with a LEVEL 1 signal are liberated and the memory cells can be overwritten.

The event memory address counter (0 - 4) is incremented by every LEVEL 1 signal. This address is called the EVENT NUMBER. Readout of an event from one of the event registers is initiated by the READ ENABLE signal. The counting of this signal determines which event register to read from. The ERROR flag is sent if a read/write operation is attempted on an event memory which is busy with another write/read operation.

All data in an event register come out as 48 serial bits. ID00 come out first and ID47 as the last bit. The event number (3 bits, the number of the actual event register) and one parity bit (even) are added to the data stream. Their output signal is driven by the read clock (RCC). RCC is the same as ICLOCK in the present tests.

Serial Communication with the ROC

The serial communication of the ROC was controlled by a test set (ROC-test) developed at Lund University based on LAB-windows software (produced by National Instruments Corporation, Austin, Texas, USA) and running on a PC .

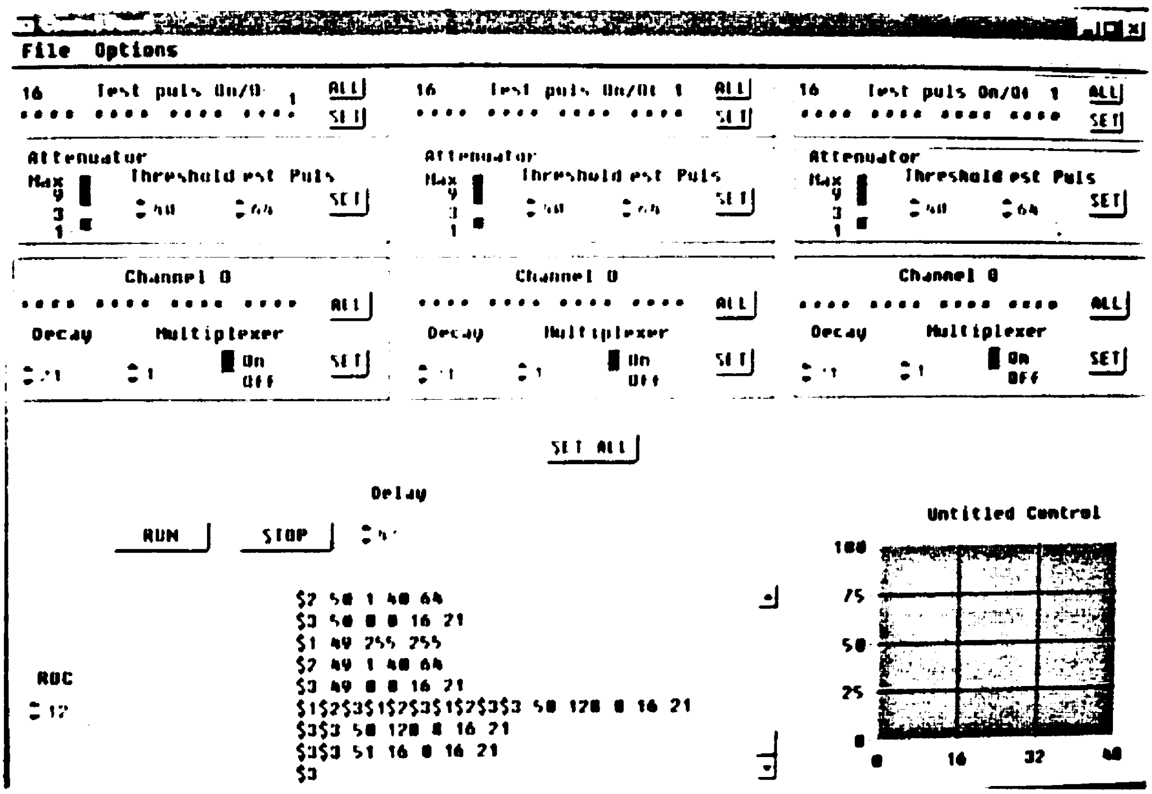

Figure 3.8: Picture of the control panel of the ROC-test program.

Figure 3.8 shows a picture of the control panel of the ROC-test and of the interface card. There are three columns of control panels, one for each chip of a given ROC card. The ROC number is specified in the bottom at the left. The top panel controls the test pulse option. The test pulse could be activated on each channel separately. The amplitude of the pulse is the same for all 16 channels of one chip, and could be controlled from the middle panel. The attenuation of the multiplexer output and the threshold of the discriminator are controlled from the middle panel and are common for all 16 channels of one chip. Each channel could be switched on and off individually. This is set from the bottom panel. There is also an option to enable the multiplexer test output, and to change the decay time, controlled from the bottom panel.

The interface card has a microcontroller and interface chips which convert into CMOS signals the input (output) RS-485 differential signals received (transmitted) on the motherboard traces. The serial string was operated at 1 MHz. A picture of the interface is shown in figure 3.9. Figure 3.10 presents the relative timing of the control signals in a typical data loading and read-out communication with a chip.

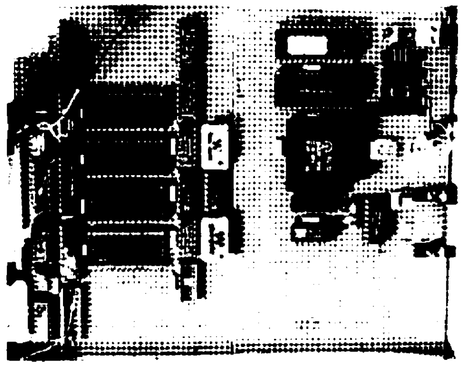

Figure 3.9: Picture of the interface card for the ROC-test.

The following is a brief explanation of the signals controlling the TGLD chip:

OS Operate/Serial Control:

- OS = 0, Operate mode
- OS = 1(non-zero, pull up), Serial Control mode, enable the serial communication.

SAD Address/Data Control:

- SAD = 1 , enable address read mode.
- SAD = 0 , data mode.

RD/SC Reset Disable/Serial Clock:

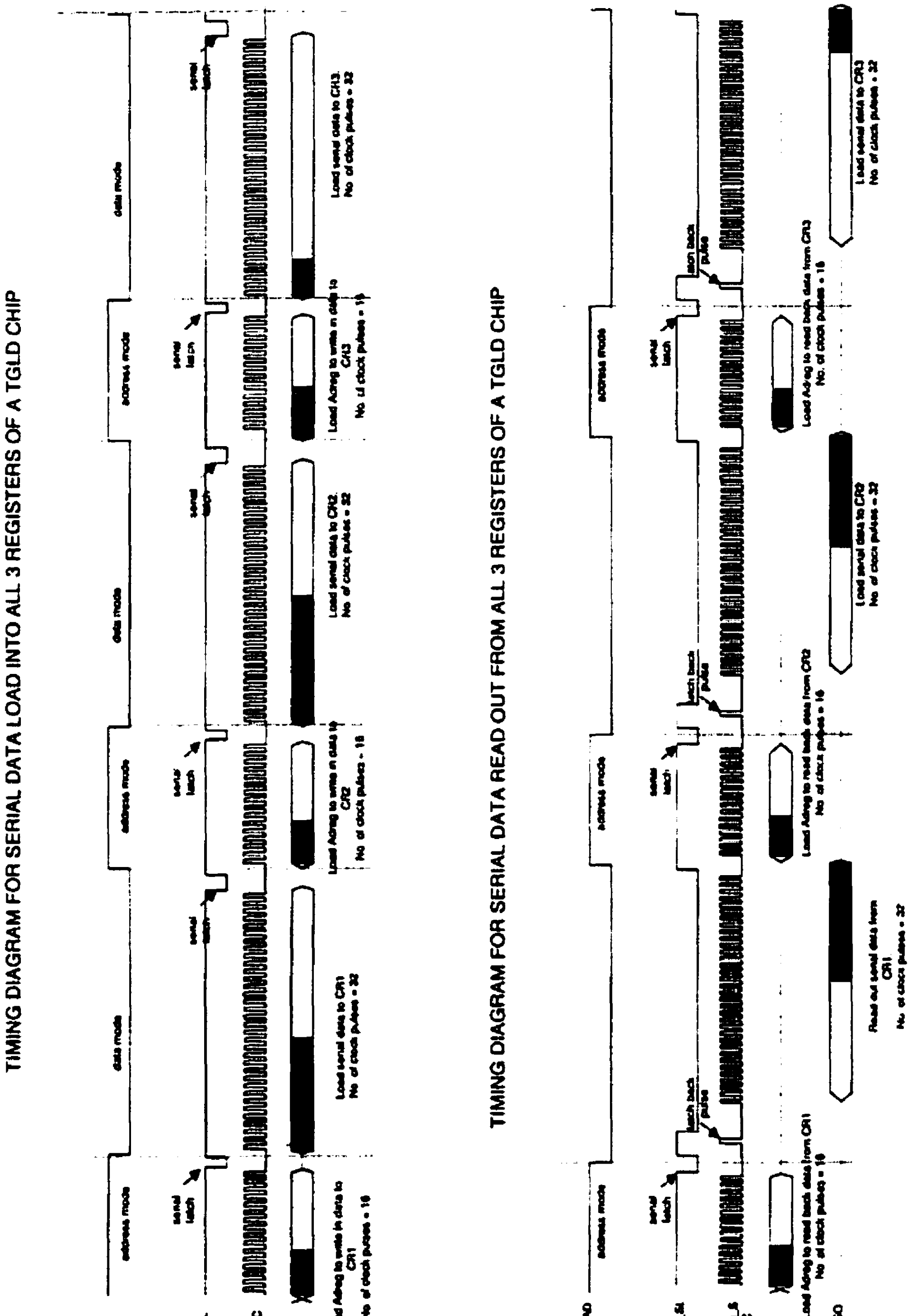

Figure 3.10: Relative timing of the control signals during the communication process with the ROCs.

- OS = 0, RD = 0 – out of reset mode.
- OS = 0, RD = 1 – reset preamplifier.
- OS = 1, Serial Clock for the data (in/out).

SOE Serial Out Enable:

- SOE = 0, receive data.
- SOE = 1, transmit data.

TP/SL Test Pulse/Serial Latch

- OS = 0, Test Pulse: inject charge in the preamplifiers. The amplitude of the TP (amount of charge injected) as well as the enabling of individual channels is controllable.
- OS = 1, Serial Latch

SI Serial Input (SOE = 0): address (SAD = 1) and serial data (SAD = 1) for the three registers of TGLD (ON/OFF, Attenuation, Threshold), 16 bits.

SO Serial Output (SOE = 1): output data from the three registers, 32 bits.

3.3.2 Electronic Control and Data Acquisition (DAQ) System

Signal Control, NIM Setup

The functionality of the detector requires several correlated signals with a timing precision of the order of magnitude of ns. The control signals are generated using a logic setup of NIM electronics assembled in two NIM crates. Figure 3.11 shows the logic diagrams of this system. The following is a description of the signals sent to the ROCs used to control the data readout.

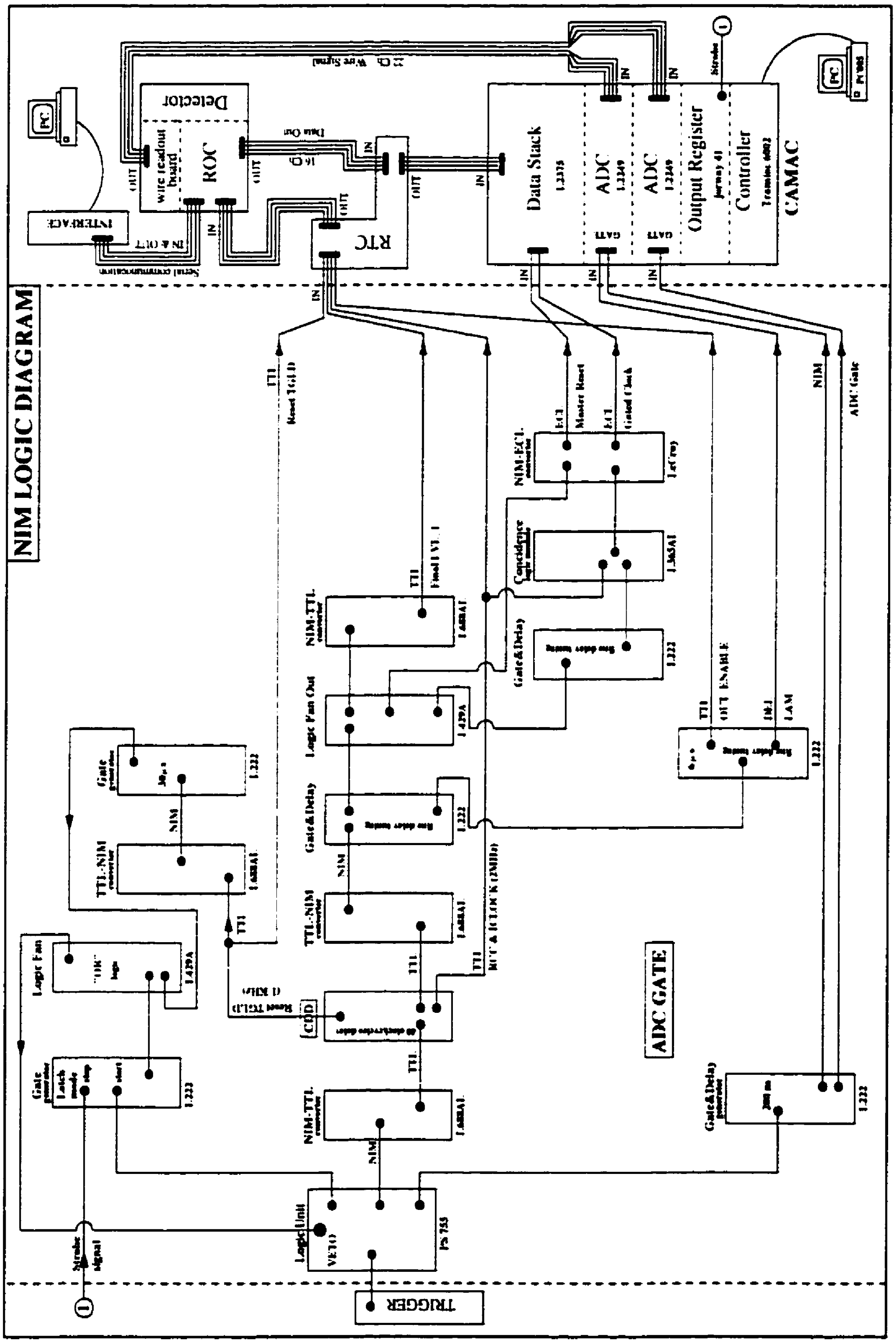

Figure 3.11: NIM logic diagram.

CLOCK: There are two clock signals requested by the ROC cards (ICLOCK and RCC). A special module (CDD) designed and built by Nick Starinski (McGill University) was used. It has three main functions:

- **CLOCK GENERATOR:** Provide a 8 MHz clock with TTL output signal used for both ICLOCK and RCC.
- **DIGITAL DELAY:** For every TTL input trigger signal it will issue a TTL output signal at the 40^{th} rising edge of the clock. The numbering starts with the next rising edge following the trigger. This way it de-randomizes the trigger in relation with the clock.
- **RESET PREAMPLIFIER:** Gives also an 1 KHz TTL pulse used to reset the TGLDs.

LEVEL 1: There were two different kind of tests pursued: one with X-ray source and the other with cosmic rays. In the first type of experiments the wire signal, amplified with a fast linear amplifier, triggers a discriminator to give the primary LEVEL 1 signal. In the cosmic rays experiments a coincidence between three scintillators is required to trigger an event. This signal is directed to a trigger logic unit. A VETO signal stops the data acquisition process if one of the following holds:

- A strobe signal from the CAMAC system have not yet arrived after the last event (the readout of the previous event is not completed).
- A RESET PREAMPLIFIER signal was sent within the last 30 μs. The reset preamplifier is sent with 1 KHz frequency and open a veto gate of 30 μs.

One output of this trigger logic unit starts a new veto gate which will be closed by the strobe signal when the readout of the event is completed. The second output starts a gate&delay generator for the ADCs used to record the wire signals. The third output passed through two delays:

- A digital delay of about 40 clock-cycles (generated by the CDD module) which also creates stability with the clock. This require a double conversion NIM-TTL, TTL-NIM.
- A variable delay is adjusted so that LEVEL 1 comes immediately after the data reach the end of pipeline.

Then the signal is converted to TTL and sent to the ROC.

OUT ENABLE: The final LEVEL 1 signal also triggers a gate&delay generator of $6\mu s$ in order to provide the OUT ENABLE signal (The signal should last longer than the serial output for 48 data bits + 4 event number bits + 1 parity bit, each bit representing 125 ns time length for the 8 MHz RCC clock used). The delay was fixed to about 2 μs relatively to the LEVEL 1 signal (the only requirement is that it should be more than 100 ns, so that the writing process in the event buffer is completed). The TTL output of the gate module is sent to the ROC.

DMU RESET: Normally a reset of the DMU is not needed on a regular basis. One reset at the beginning of each run should be enough. However, because errors at the event counter have been noticed in our test, a DMU RESET was sent after each event readout. It is obtained by triggering a discriminator from the falling edge of the $\overline{NIM}$ signal of the gate generating the OUT ENABLE signal. This way we assure that the reset is coming after the event readout is completed.

Diagrams of the relative timing for several of the relevant signals are shown in figures 3.12, 3.13, and 3.14

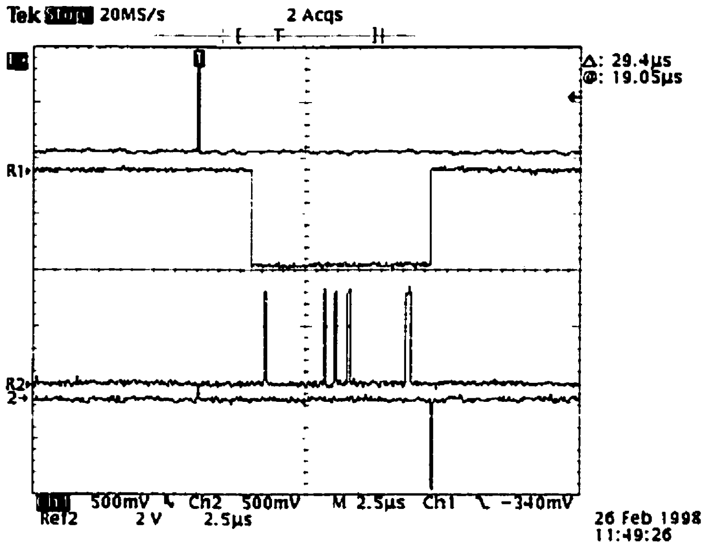

Figure 3.12: Example of control signal relative timing. **Ch. 1** (label "1" in the figure): LEVEL 1 delayed: **Ch. 2** (label "2"): serial data out (typical event): **REF. 1** (label "R1"): OUT ENABLE signal: **REF. 2** (label "R2"): reset DMU.

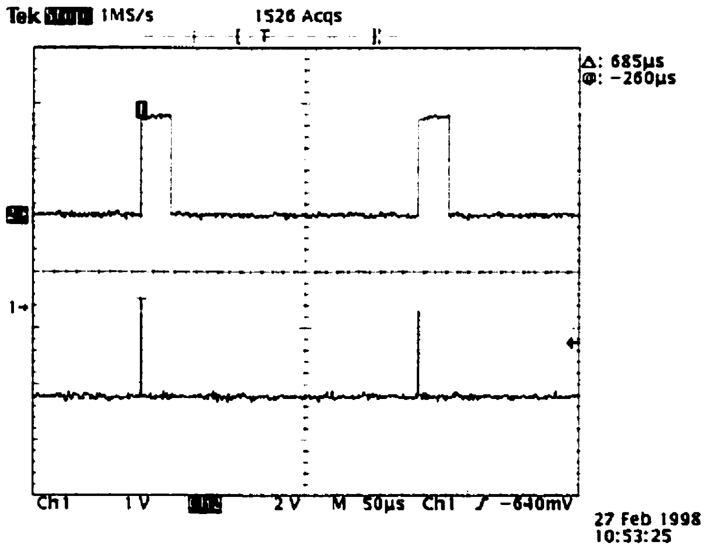

Figure 3.13: Example of control signal relative timing. **Ch. 1**: reset preamplifier: **Ch. 2**: veto gate.

CAMAC Assembly and Interfaces

Specially designed Front End Module (FEM) cards will be mounted at one edge of the chambers in the final pad detectors to be installed at RHIC. They work as

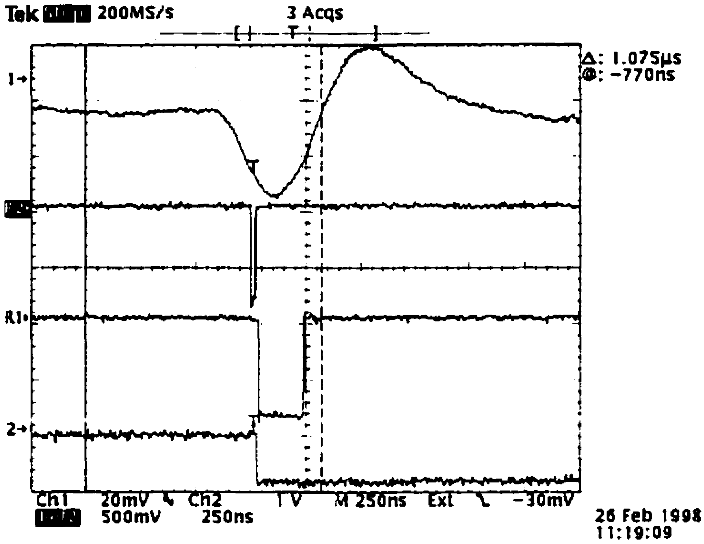

Figure 3.14: Example of control signal relative timing. **Ch. 1**: wire signal; **Ch. 2**: veto gate; **REF 1**: ADC wire readout gate; **REF 2**: LEVEL 1 primary, triggered from wire signal.

interfaces for the control signals of the ROCs. As a substitute for the FEM card a receiver-transmitter card (RTC) with LTC 489 receiver and LTC 487 transmitter chips was built. It was fixed at the edge of the chamber. The RTC card converts the TTL input (output) signals into RC-485 differential signals to be sent to (received from) the ROCs through the motherboard lines. Differential signals were prefered to single ended signals used in previous prototypes. The purpose is to reduce the noise induced mostly by the capacitive couplings between the motherboard traces and the cathode pads.

The data is readout by a CAMAC based acquisition system. A CMOS to TTL converter receives CMOS pulses from the RTC interface card and converts them to ECL. The data are then feed into a DATA STACK. Two signals should be provided to the "data stack":

MRST : Master Reset (ECL) pulse resets the internal read and write pointers. It is sent, from the final LEVEL 1 signal converted to ECL, before the data reach

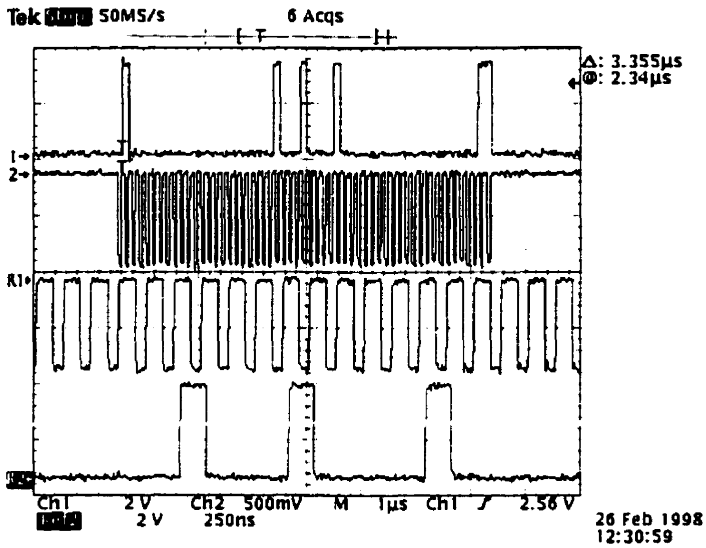

Figure 3.15: Relative timing between data (**Ch. 1**) and the WE signal (**Ch. 2**) provided to the "data stack" module. The same, but with different time scale, is shown in **REF 2** and **REF 1** respectively.

the "data stack".

WE : Write Enable (ECL) initiates a write cycle. The leading edge of this pulse writes the data-word present at the "DATA IN" connector into the memory addressed by the write pointer (WP), and advances the WP. We get this signal by a coincidence between the clock and a gate generator. The signal is passed through a delay module which permit to adjust the timing and then it is converted to ECL. Figure 3.15 shows the timing between WE and the serial data of a typical event at the "data stack" input.

A Look-At-Me (LAM) signal is provided from the "delay" output of the OUT ENABLE generator gate into an ADC module of the CAMAC crate. Two CAMAC ADCs (12 channels each) are used to readout the anode charge of the 22 wires of the detector. Another ADC is used to readout all three analog outputs of the scintillators in cosmic rays tests.

The software used to control the CAMAC was the SUSIQ V7.01 DAQ program

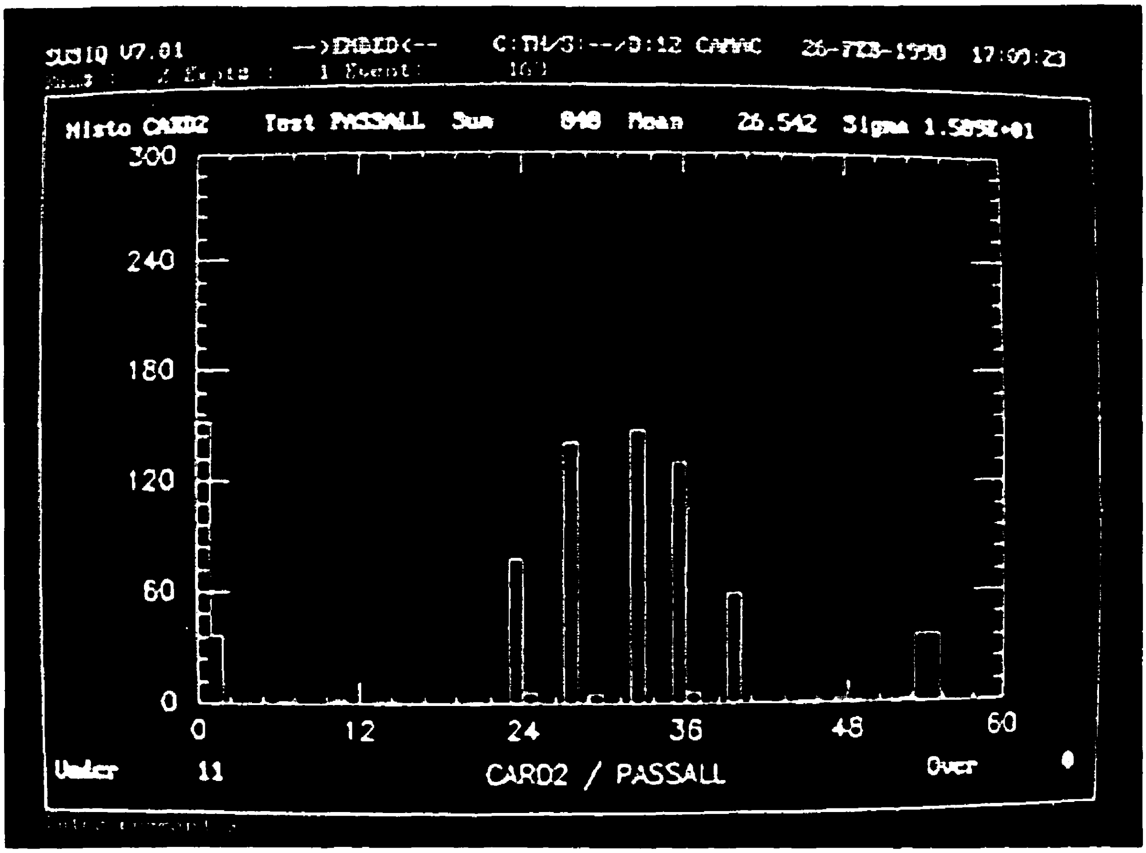

Figure 3.16: Example of data acquisition display. This histogram is typical of those filled during typical X-ray runs.

developed by a TRIUMF collaboration. It was running on a PC. Figure 3.16 shows a typical display of a histogram filled during the DAQ process. The histogram shows the 48 channels of a readout card. It was filled during a typical X-ray run. For each event the histogram is filled with the fired pads. In this example most of the time 3 pads, comprising one cell, are fired. The event number (4 bits) and the parity bit could be seen at the beginning and the end of the 48 channels respectively. A Transiac 6002 was used as CAMAC crate controller, coupled to a Transiac PC005 interface card mounted in the computer.

3.3.3 Wire Signal Readout

In the prototype, a wire readout signal was included. The measurement of the wire signal has many advantages including:

- Provides information on the charge deposited by the particles passing through the detector.
- The gain of the chamber could be monitored.
- The wire signal could be also used for triggering events in the test with X-rays when no external trigger could be used.

For this purpose a special readout board has been designed and is schematically shown in figure 3.17 (top).

Because the charge produced by an avalanche and collected by the anode wire is large we keep only 1/6 of the anode charge. A charge divider consisting of two parallel capacitors of about 1/5 capacitance ratio is used to discard about 5/6 of the anode charge.

A charge sensitive preamplifier forms the second stage of the wire signal processing. A BNL-IO-456-4 low noise, high performance preamplifier was used. It is an inverting preamplifier with a feedback loop through a capacitor. It converts the input charge to a voltage output. Its gain is determined by the feedback capacitor. The output voltage is proportional to the input signal charge. The gain of the preamplifiers have been measured to be about 54 mV/fC.

Preamplifiers' output has a rather long decay time ($10 - 100$ μs typically). To reduce the signal time-length, pulse shaping amplifiers are used to process the preamplifiers' output. They consist of delay line clipping, or R-C, C-R networks, thus they are shaping the pulse while keeping the linearity between input and output pulses. 200 ns BNL-IO-533 bipolar shaping amplifiers were used for this purpose. A photograph of the preamplifier and shaper is shown in figure 3.17 (bottom).

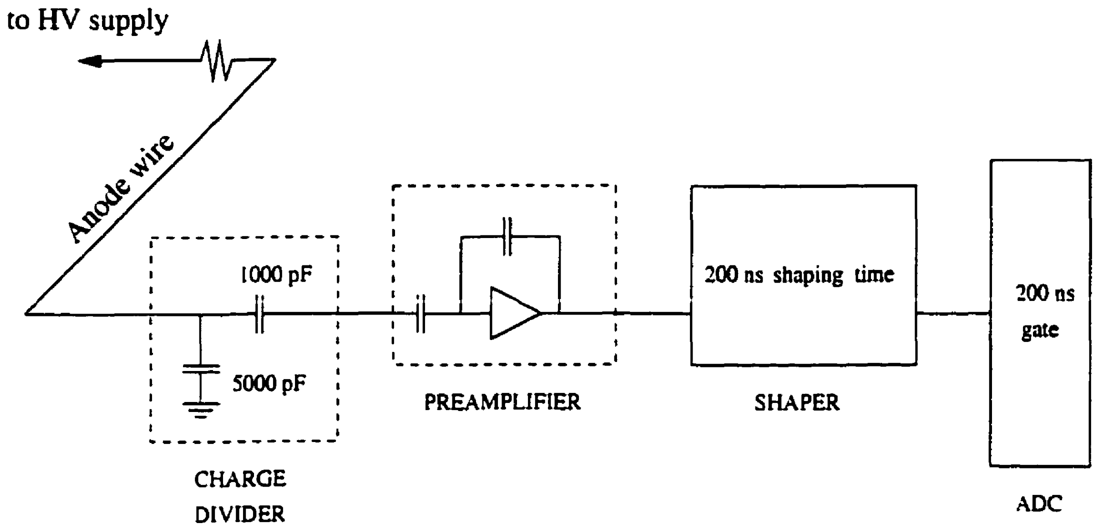

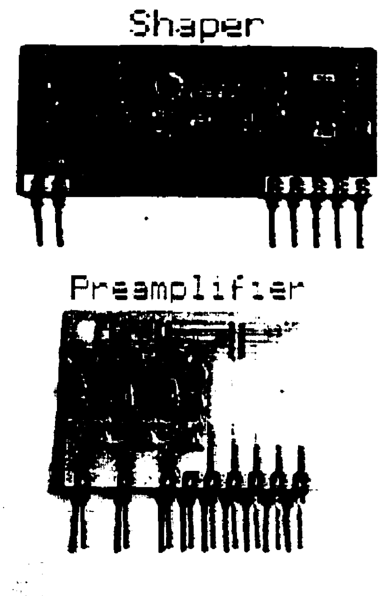

Figure 3.17: (**top**) Wire readout logic diagram. (**bottom**) View of the preamplifier and shaper.

The outputs of the shaping amplifiers were connected to an analog to digital converter (ADC) which convert the analog pulse into digital information used later in the data analysis. The ADC was provided with a 200 ns gate. A typical preamplifier output, shaper analog output and the correlated gate signal for ADC, in a pulser generated event, is shown in figure 3.18.

3.3.4 Detector Calibration

In order to determine quantitatively the gain of the detector, a calibration system has been built. A pulser was used to charge a capacitor which is then discharged through the wire readout system. A logical scheme of the calibration set-up is shown in figure 3.18. Because the input charge in the wire readout system is relatively small (about 100 fC) a charge divider formed by two parallel capacitors is used in the front of the calibration capacitor. The analog output of the wire signal is digitized by an ADC and readout through the CAMAC based data acquisition system. The input charge is computed from the input voltage and the known values of the capacitors.

The linearity and the gain have been studied during the calibration process. The results presented in figure 3.19 show very good linearity of our wires readout system. The gain, expressed in ADC counts per fC input charge, is shown in the second part of figure 3.19 for all 22 wire channels. The values of the capacitors used to divide the anode charge have an uncertainty of about 20% and may explain the observed differences in gain.

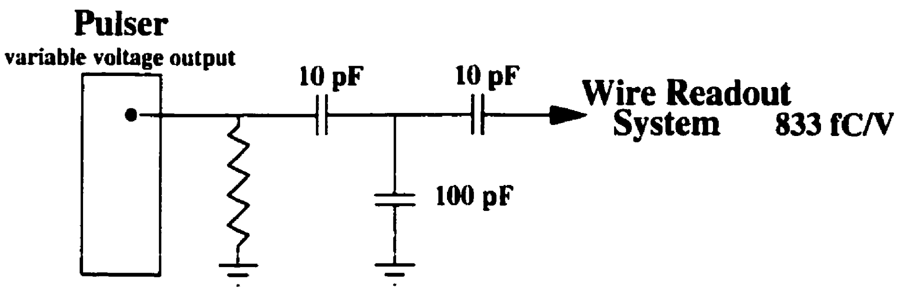

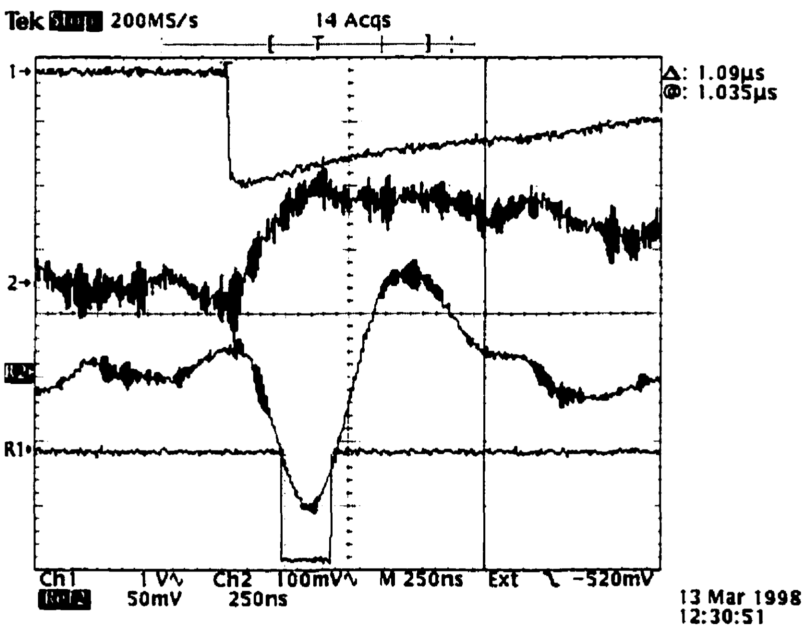

Figure 3.18: Calibration setup and signals. (**top**) Calibration setup logic diagram. (**bottom**) Several relevant signals are shown. **Ch 1** (label "1" in the figure): input signal from a pulse generator. **Ch 2** (label "2"): preamplifier output. **REF 2** (label "R2"): shaper amplifier output. **REF 1** (label "R1"): 200ns gate for ADC.

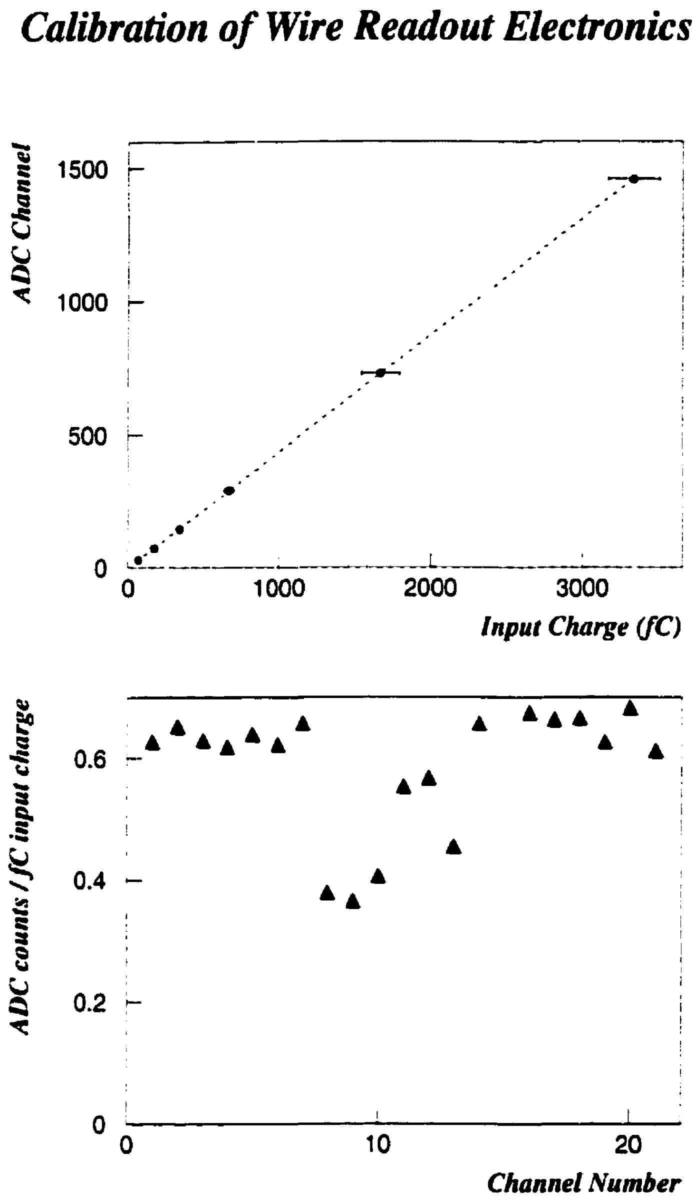

Figure 3.19: Calibration data. (**top**) ADC channel versus the charge input (fC). (**bottom**) The wire readout gain, expressed in ADC counts per fC input charge, for each channel of the wire readout.

Chapter 4

Experimental Results

Two kinds of tests of the detector have been pursued at McGill University between August 1997 and March 1998: cosmic ray and X-ray tests. This chapter will present the result of these tests. Some of the results will be compared with Monte Carlo simulations in the next chapter.

4.1 Test of the prototype operation as a MWPC

Before we will proceed with a discussion on the tests of the prototype performances, we will study the operation of the detector as a MWPC. Some characteristics will be studied with our attention focused on the gain.

The anode charge spectra of the ^{55}Fe X-ray source is narrow, therefore, it is appropriate to study the dependence in the gain of the chamber. Because for a typical MWPC the gain is expected to be exponential with the anode high-voltage (HV), the relationship is linear up to some saturation point when plotted in logarithmic scale. Figure 4.1 presents the anode charge dependence on HV for wire # 11 of our prototype. A good linearity is observed and the saturation point is not attained below 2030 V, the upper limit of the tests. As shown in the figure a similar dependence with HV is obtained with cosmic rays when we follow the shift of the Landau distribution peak of the anode charge. The gain has to be the same but with a different absolute value. There is a difference of a factor of $5-6$ between the magnitude of the anode charge signal for X-rays and cosmic rays. This is consistent with the energy ratio deposited in the active volume of the detector by the ^{55}Fe X-ray source and 1 GeV muons [46, 47] (cosmic ray muons have the average energy about 1 GeV).

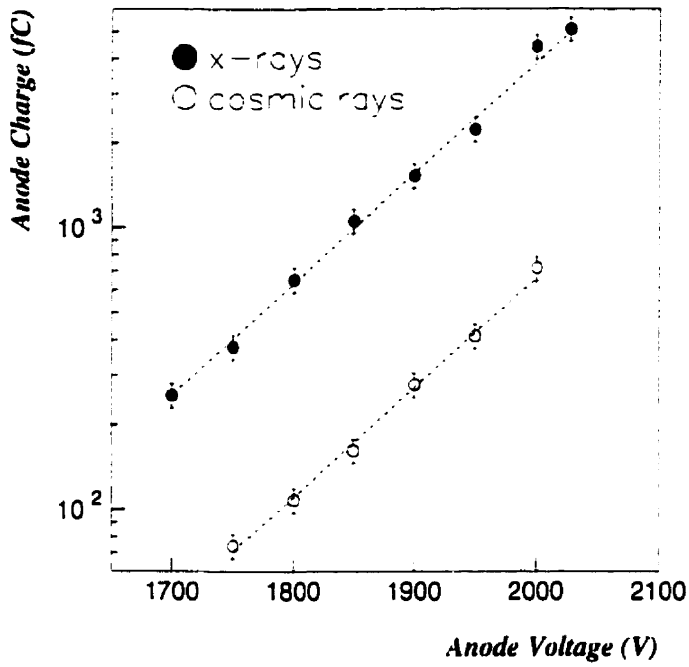

Figure 4.1: Anode charge dependence on the anode voltage. (full circles - "•"): The variation with HV for X-rays measurements; (empty circles - "o") the same variation for the peak of the Landau distribution generated by cosmic rays.

To evaluate the stability of operation of the chamber we have also studied the gain dependence with the gas flow rate. The gas used in our test was a mixture of 50% argon-50% ethane Figure 4.2 shows a schematic view of the gas flow control system. Two "Cole Parmer" flowmeters measure the argon and ethane gas input flow into a mix-chamber. The mixture is then directed to the detector. A "Matheson" flowmeter measure the gas output from the detector. No difference between the amount of gas input and output was noticed, indicating that the gas chamber of

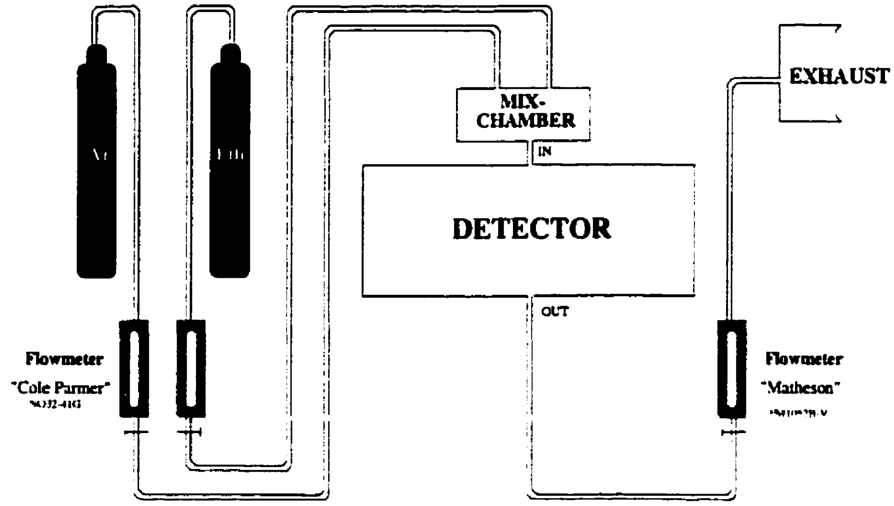

Figure 4.2: Gas mixture setup.

the detector is very well sealed. In all tests we used this gas mixture. The same gas mixture is expected to be used in the PHENIX experiment. The flow rate was changed from 21 ml/min up to three times this value, while keeping the same gas mixture. The flow in the PHENIX experiment, when normalized to the volume of the prototype, is planned to be in the range of $30 - 40$ ml/min. The results, plotted in figure 4.3, does not show any perceptible variation in the gain. The chamber operation was stable so we decided to keep a low flow rate of 21 ml/min for all tests.

4.2 Particle Hit Identification

For the evaluation of the detector performances we needed to process the raw data in order to identify and study the characteristics of the particle hits. The raw data from the tables produced by the acquisition are reordered in arrays with respect to the geometrical order of the pads. Once the mapping is done the analysis programs will search for fired cells. Only the cells with three pads above threshold are considered to be fired. The cells fired are geometrically ordered in arrays and a cluster reconstruction will follow. A cluster is a group of one or more adjacent fired cells. For large

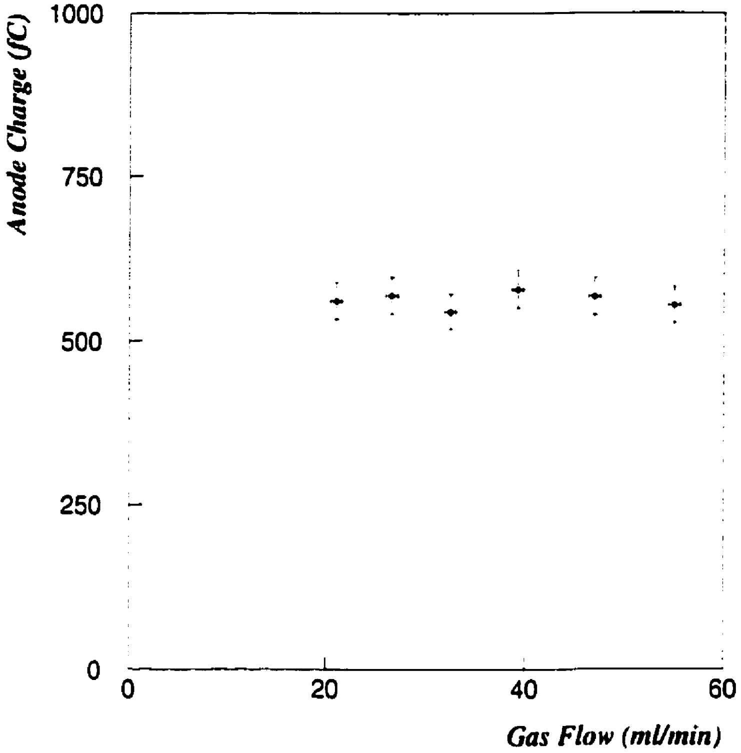

Figure 4.3: Anode charge dependence on the gas flow.

avalanche size it was observed that more than one cell are fired. The experimental data as well as the simulations shows several types of reconstructed clusters. In the limit of 3×3 cells for the cluster size, a classification of the cluster type used in the analysis is presented in figure 4.4. The final position resolution is related with the type of the cluster. The cluster type itself is directly related to the number of the fired cells. The efficiency is another important detector characteristic. *E*fficiency is defined as the ratio of the number of events with identified clusters to the total number of events. Therefore it is important to study how the number of fired cells and efficiency vary with the operational parameters (like the threshold and HV).

The programs take into consideration the dead pads in the following manner. All dead (hanging, noisy) pads are switched "off" (considered not fired; there were about 3% of the pads in this situation). If we are able to identify the hit (find a cluster) we

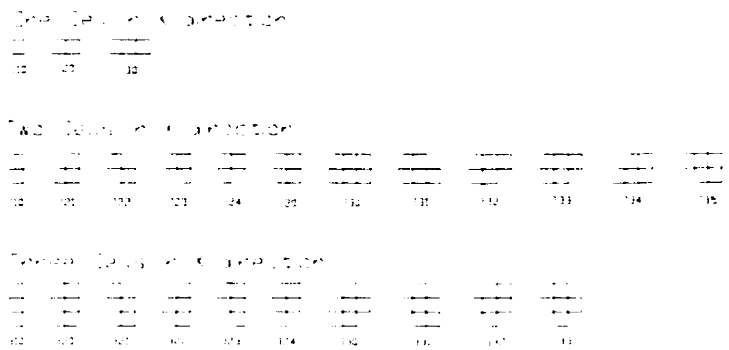

Figure 4.4: Cluster Types. The numbers below label each cluster type. The first (second) digit shows the number of fired cells in x (z) direction. The third digit label the cluster in each class (same two digits).

will stop the algorithm. If not, we switch "on" (consider fired) one dead pad and we look again for clusters. If we fail again to find a cluster we switch "off" this pad and switch "on" another dead pad. We follow this procedure until we identify the hit or we have scanned all the dead pads (in which case an "empty" event is recorded). In this way the reliability to have a fired cell will remain on three, minimum two, pads.

All analysis codes are written in FORTRAN and were running on a UNIX machine (Silicon Graphics). The data transfer between computers was accomplished using FTP facilities. The final analysis of the data was done using the PAW (Physics Analysis Workstation) developed at CERN [48].

4.3 X-Ray Tests

A special stand was designed and built to hold the X-ray source. Figure 4.5 presents a picture of this device. It allows the positioning of the source with a precision of less than 1 mm in both dimensions, x and z. The ^{55}Fe X-ray source is encapsulated in a steel case which has a small circular opening ($\phi = 1\ mm$) to produce radiation that is collimated. The geometrical position of the source inside the case gives a radiation

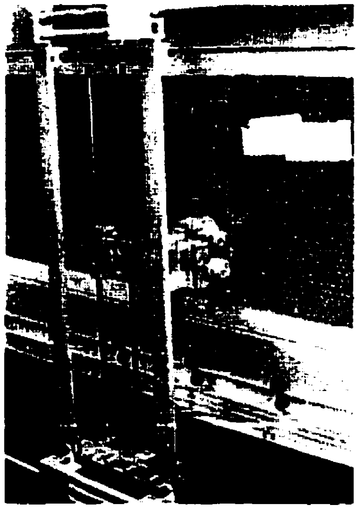

Figure 4.5: X-ray test setup.

angular spread of about 45^0. The distance between the X-ray collimator and the anode plane is about 1 cm resulting in a radiation spot at the anode wire level of about 1 cm. The surface covered by a single readout card is thus large enough to detect all possible X-ray events in a given test run.

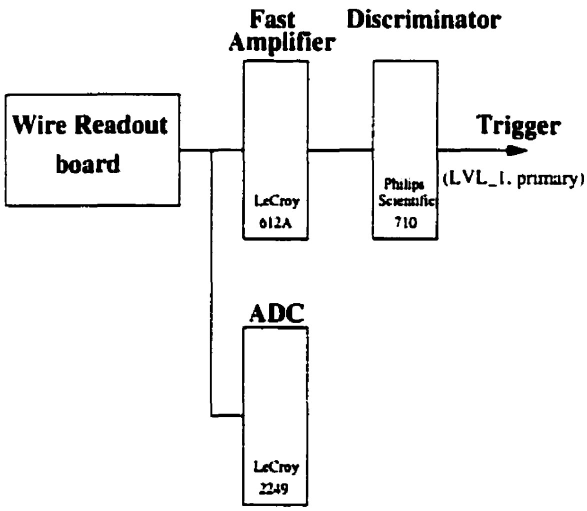

Figure 4.6: X-ray test trigger setup.

For the X-rays tests the wire signal is used to trigger the readout system. A schematic view of the trigger set-up is shown in figure 4.6. A fast amplifier is used to amplify the wire signal. A discriminator, whose threshold is set just above the noise, gives the primary trigger to the NIM electronics. The counting rate of the triggered events is about 5 events/sec. Besides the X-ray events there is a non-negligible background, mostly from cosmic rays which hit the detector in an area of the detector not covered by the readout cards. All results are presented after the subtraction of a normalized background.

A typical X-ray anode charge spectra for 1800 V high voltage is presented in figure 4.7. One of the advantages of X - rays tests is that we have a good statistics

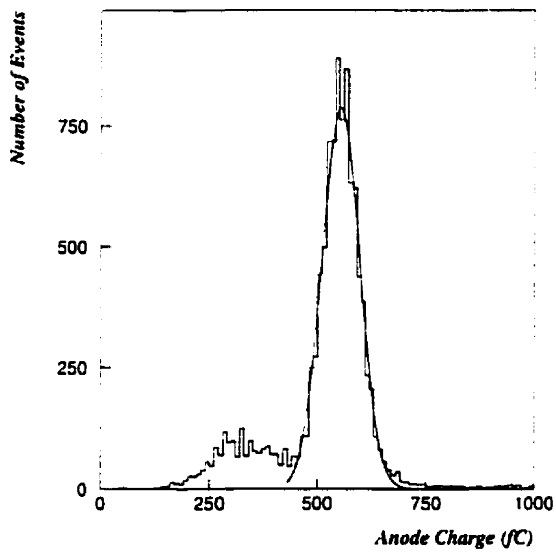

Figure 4.7: Anode charge spectrum for an X-ray test. The anode voltage is 1800 V.

for events which produce anode charges with a narrow amplitude distribution. The main peak in the spectrum has a Gaussian shape. In these tests, only those events with an amplitude corresponding to the peak position ($\pm\sigma$) are kept in the analysis. The integrated pattern of pads and cells fired for one position of the X-ray source is shown in figure 4.8. The distribution of pads and cells fired per event is shown in figure 4.9. We observe that mainly 3 and 4 pads are fired. They are reconstructed in one or two cells respectively. The adjacent cells are also fired mainly because the radiation from the source cover more than one cell.

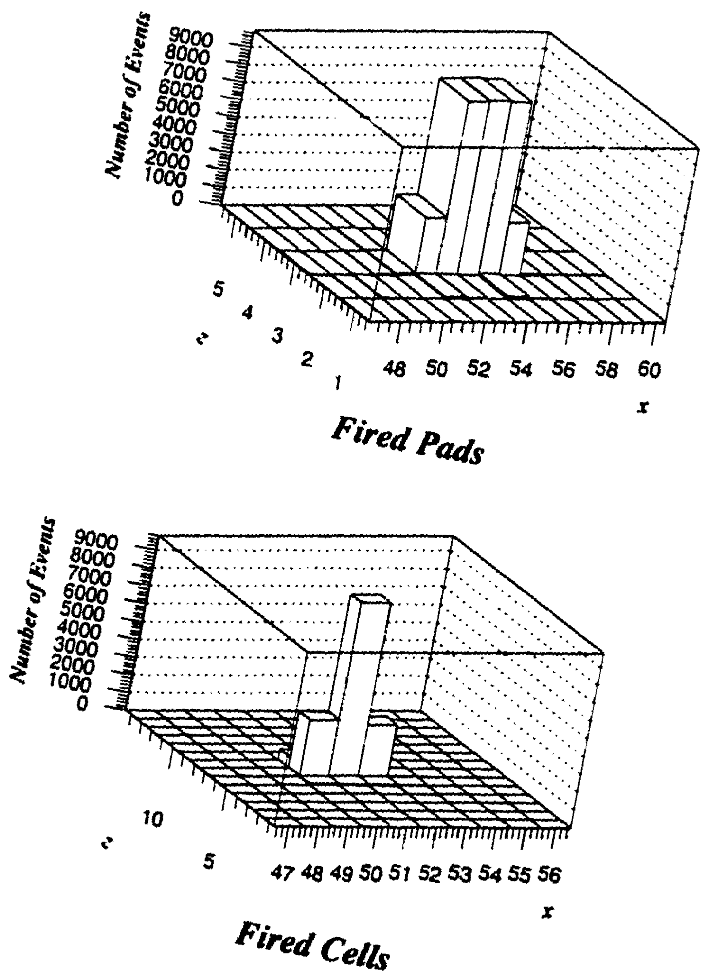

Figure 4.8: **(top)** The figure shows the geometrical distribution of fired pads. **(bottom)** This figure shows the same for fired cells.

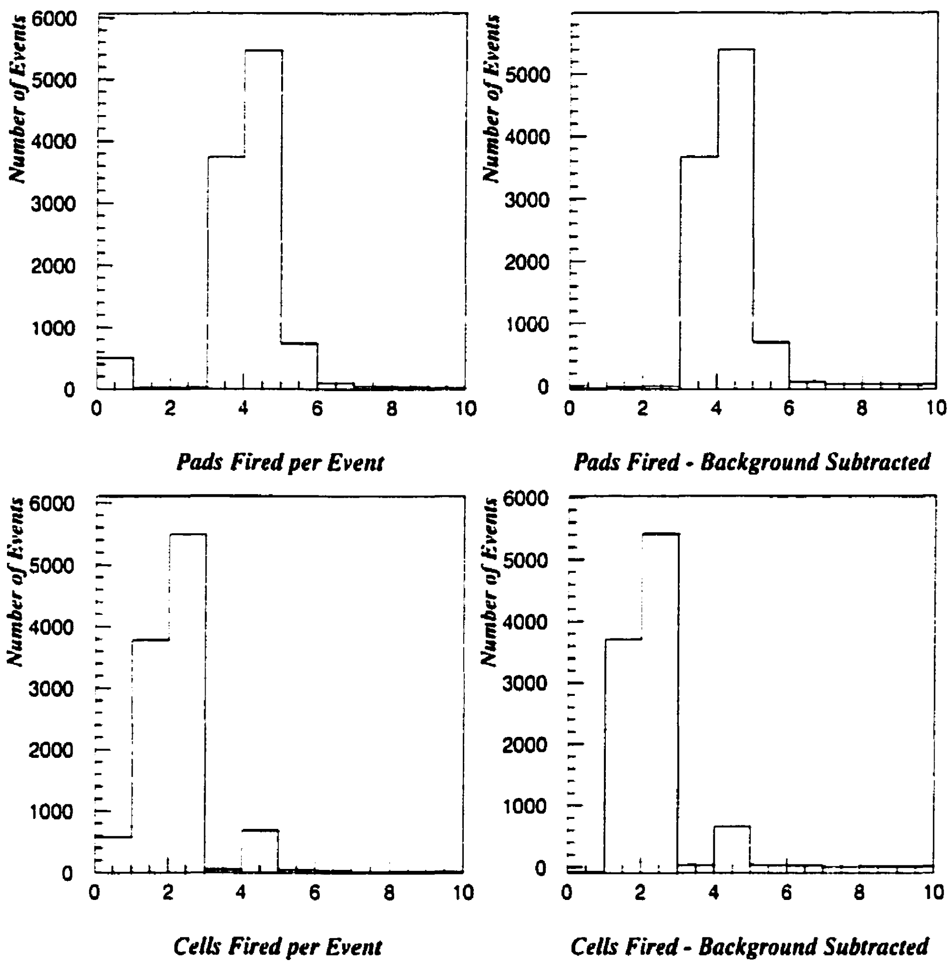

Figure 4.9: (**top**) The figures show the statistical distribution of number of fired pads per event. (**bottom**) The figures show the same for cells. X-ray test, $HV = 1800\ V$.

4.3.1 Detector Response as Function of the Anode Bias

A systematic study of the response of the detector as a function of the anode voltage has been done. The threshold was fixed to 3.9 fC. Figure 4.10 (top) shows the efficiency dependence on the anode voltage. The efficiency is practically 100% for HV greater than 1700 V and abruptly decreases (we will call this the "breaking point") at lower voltage. The background subtraction introduces some uncertainty.

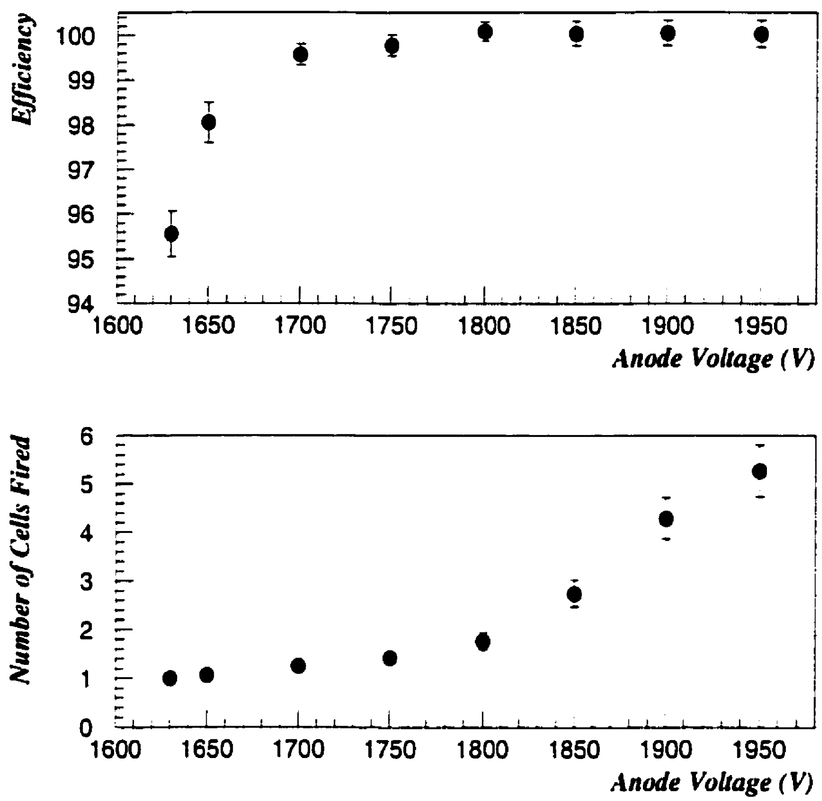

Figure 4.10: **(top)** The figure shows the efficiency dependence on HV in X-rays tests. The threshold is 3.9 fC. **(bottom)** The figure displays the average number of cells fired for the same set of tests.

Therefore it is possible to have the most probable value of the efficiency greater than 100% for some measurements. In the same figure (bottom) the average number of cells fired per event are plotted as function of the anode voltage. The average number of cells fired is relatively small and increase linearly with the anode voltage up to about 1800 V. For anode voltages greater than this value, the cluster size begin to increase relatively rapidly with voltage.

4.3.2 Detector Response as Function of Threshold

Two sets of tests with two different anode voltages (1650 V and 1850 V) have been done. The results are plotted in figure 4.11. For the measurements at 1850 V, only the data representing the average number of cells fired is presented since at that voltage the charge is relatively large and, for the threshold used, the efficiency

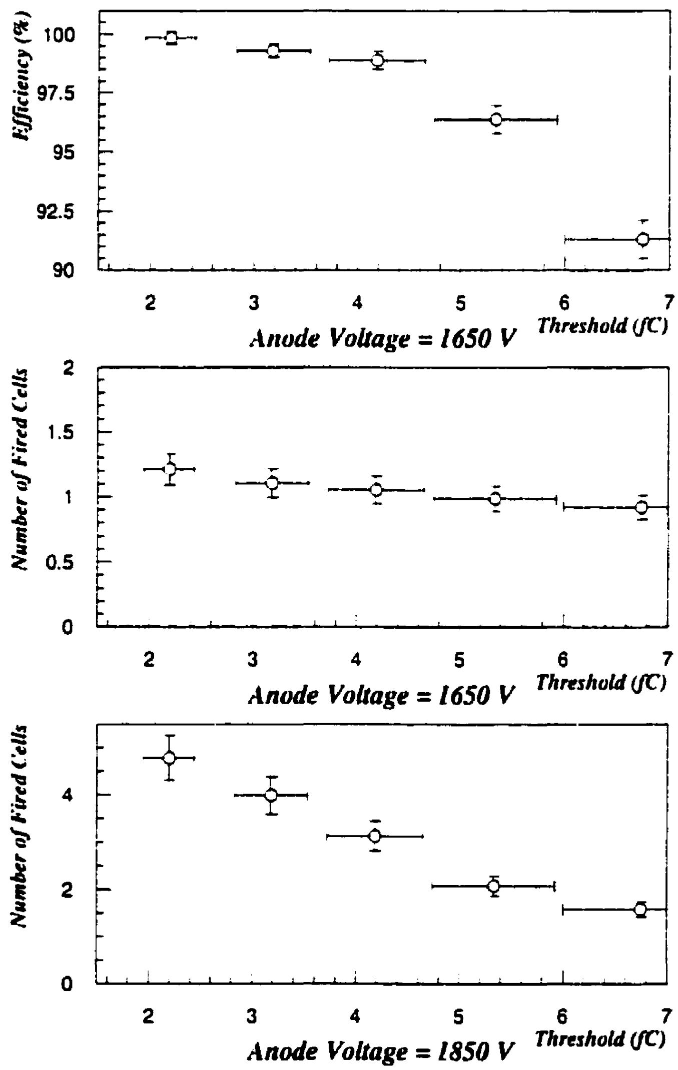

Figure 4.11: **(top)** The figure shows the efficiency dependence on threshold in X-rays tests, $HV = 1650\ V$. **(middle)** The figure displays the average number of cells fired for the same set of tests. **(bottom)** The figure presents the average number of cells fired for X-ray tests with $HV = 1850\ V$.

is practically 100% (within experimental errors). The efficiency data shows same similarities with that of figure 4.10, the breaking point being at about 5 fC (for the runs with $HV = 1650\ V$). The average number of cells fired per event shows the same behavior as well: the average cluster size increase linearly up to a point where it rapidly increase with the anode voltage.

It is interesting to compare the three sets of tests between them since, if the electronic noise is negligible, only the ratio between the threshold and anode wire signal should matter. The consistency of the data is shown in figure 4.12, where all the

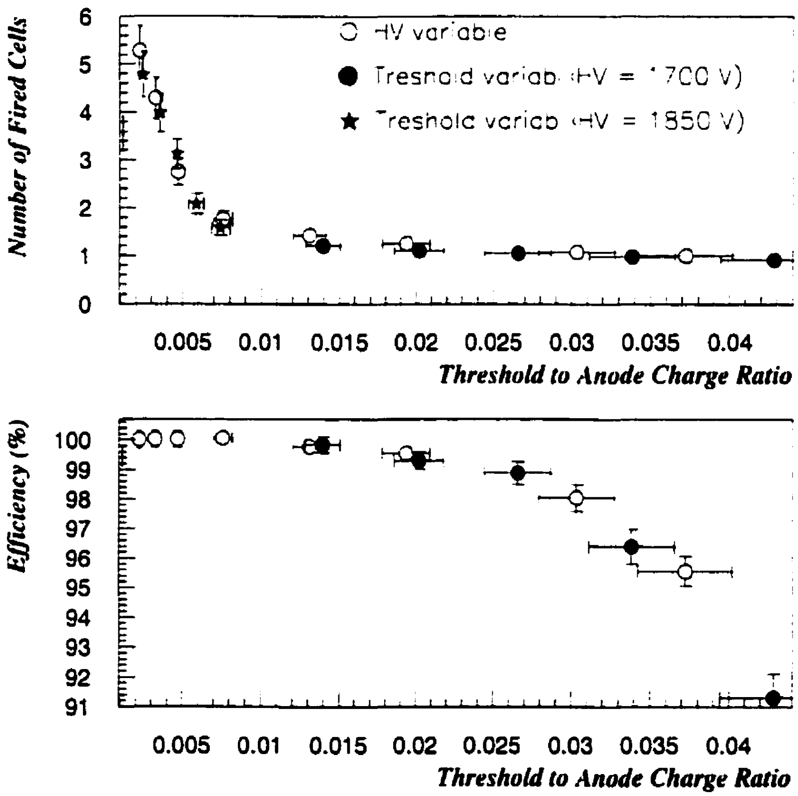

Figure 4.12: Comparison between the X-ray tests. (**top**) The figure shows the efficiency dependence on the ratio of threshold to anode charge. (**bottom**) It displays the average number of cells fired. For both pictures the empty circles ("o") shows results of the tests in which HV is the variable (*thethreshold* is kept constant at 3.9 fC). The full symbols shows results where the threshold was varied ("•" for $HV = 1650\ V$, and "⋆" for $HV = 1850\ V$).

data are plotted as a function of the threshold to anode charge ratio. It is interesting to observe that there is a plateau (0.008 to 0.027 for threshold / anode charge) where the efficiency is close to 100% while the clusters are still small, slightly above 1 cell fired per event. This clearly would be the optimum region to operate the chamber.

4.4 Cosmic Ray Tests

Only six readout cards were available and have been mounted on board in the positions 7 – 12 (for this numbering see fig. 3.2). So, the active area of the detector readout was a rectangle of 32×22 cells. The absolute limits of this area, in the cells numbering, are: $1 - 22$ (x direction) and $35 - 66$ (z direction). From now on, when we will refer to the detector, we will understand the active area covered by the readout cards.

In the cosmic ray tests an external trigger was used. Three scintillators (Hamamatsu H5010) are used for trigger purposes. Figure 4.13 shows a schematic view of the set-up for cosmic ray test and the trigger logic. The detector is placed horizon-

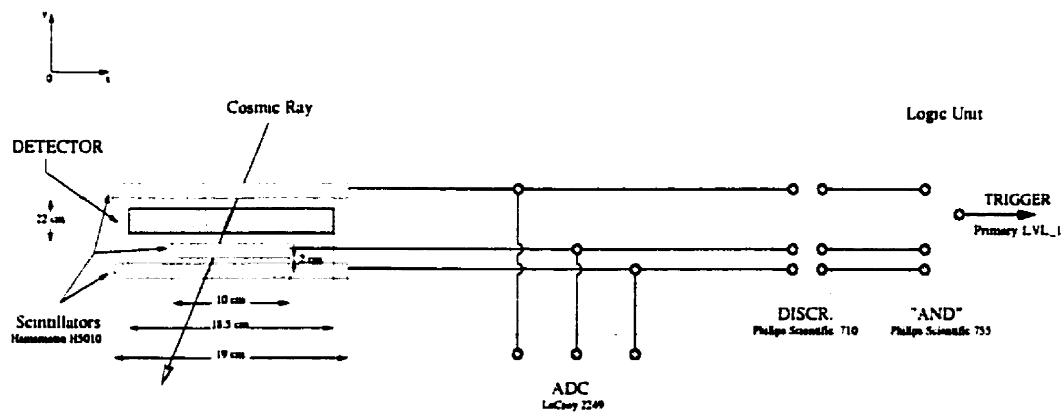

Figure 4.13: Schematic view of the setup for cosmic ray tests.

tally. One scintillator is placed above the detector and two beneath. The active area of one scintillator is a rectangle with the dimensions 10×20 cm. The top scintillator is arranged with the long side in the x direction. The two bottom ones were centered relatively to the top one and were arranged so that they formed a cross, with 2 *cm* distance in between. The scintillators were centered relatively to the active area of the detector.

The scintillators analog output is connected to a discriminator module. The discriminators threshold was fixed just above the noise. An "and" logic unit provide a primary LEVEL 1 trigger if a coincidence between the three scintillators is present. Each detector has a counting rate between 1 and 20 counts per second. This lead to a negligible rate of random coincidences between the detectors. This was tested by looking at the coincidence rate when the detectors were arranged so that no cosmic ray could traverse the three detectors. A linear amplifier was used to amplify the scintillators output and they were digitized by an ADC module. A 50 *ns* gate was provided to the ADC. Figure 4.14 display a histogram of a typical signal distribution in one of the scintillators. If one of the scintillators signal for an event is greater than 5 or less than 0.2 times the most probable value, then the event is rejected.

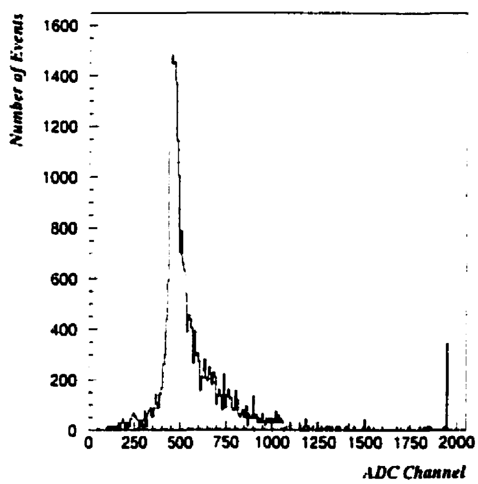

Figure 4.14: Typical scintillator ADC spectrum.

The charge deposited by the incident particle and multiplied by the avalanche is expected to give a Landau distribution (see eq. 2.2). A typical distribution in one anode wire fitted with a Landau function is shown in figure 4.15 (left side). The second plot of figure 4.15 (right side) shows the distribution of fired cells projected

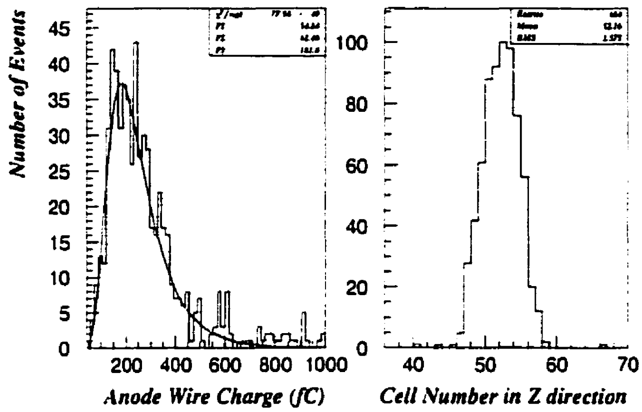

Figure 4.15: (**left**) Typical anode charge distribution for anode wire #15 obtained with cosmic rays. The distribution is fitted with a Landau function (solid line). (**right**) Distribution of fired cells along this wire.

along a wire. The peak is at the cell #52. This shows that the scintillators were placed about in the middle of the active area (in the z direction). In the same picture one could notice that the length of the area with cell fired (in z direction) is about 13 cells. This corresponds to about 12 *cm*, slightly above the 10 *cm* - the smallest length of the scintillators in z direction. This is due to the angular distribution of the cosmic rays, the scintillators being not very close to the detector. It is also expected to have few fired cells out of the active area originating from large clusters produced by hits at the edge of the active area (see below). All the results presented in this section are taken from the analysis of a test performed with a discriminator threshold of 3.9 fC and 1850 V anode voltage. These settings are normal settings, away from the limiting settings and from the settings where we have low performances of the detector (see the next two sections).

A typical pattern of the pads fired by cosmic rays is presented in figure 4.16. This pattern shows a very smooth distribution. No pad has an outstanding number of firings. This shows that there were no undetected noisy pad channels. Figure 4.17 shows the geometrical pattern of reconstructed cells. Again the pattern varies smoothly, which means that there was no reconstructed cell fired on noise. Actually, this was

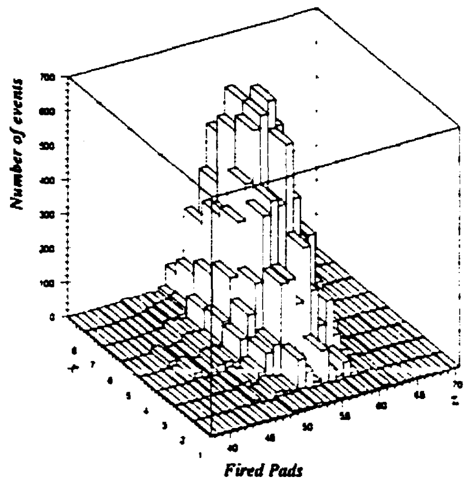

Figure 4.16: Typical geometric distribution of fired pads obtained with cosmic rays.

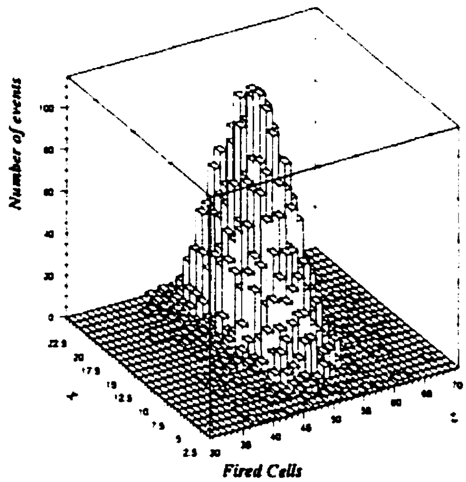

Figure 4.17: Typical geometric distribution of fired cells obtained with cosmic rays.

carefully checked with a random trigger from a pulser, and no fired cell was noticed. One could notice that the scintillators were not perfectly centered in x direction, since the patterns of pads and cells fired are slightly shifted to higher numbers. There are more hits in the center of the detector, since the central points have a larger effective solid angle for cosmic ray hits than the edge points. The points displaced toward one edge have a geometrically restricted solid angle (by the scintillators arrangement) for cosmic ray hits.

The distribution of the number of fired pads and reconstructed cells per event is shown is figure 4.18. We see that most of the events have 3 fired pads, reconstructed

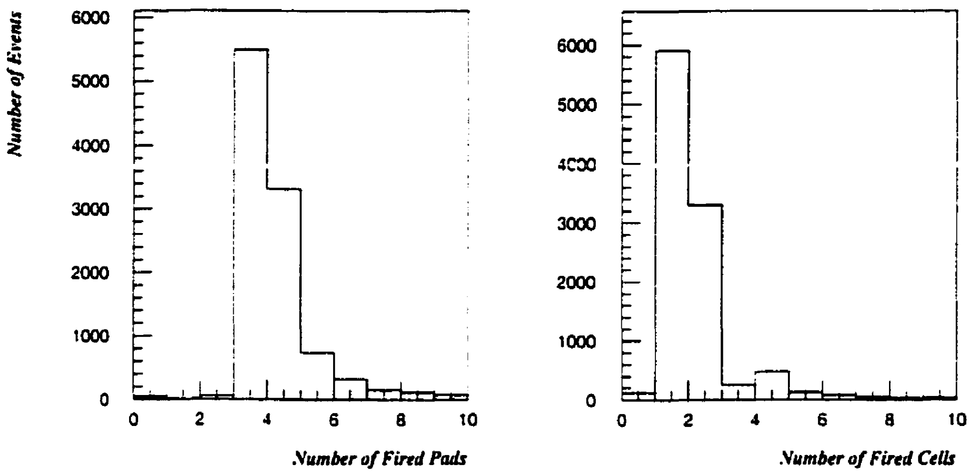

Figure 4.18: A typical distribution of the number of fired pads and cells per event in a cosmic ray test.

in one cell. There are some "empty" events, with no fired cell , corresponding to events with 0, 1 or 2 fired pads. They correspond to a loss of efficiency. There is also a significant number of events with more than one fired cell. The distribution of clusters is presented in figure 4.19. Most of the time clusters with 1 cell (pattern

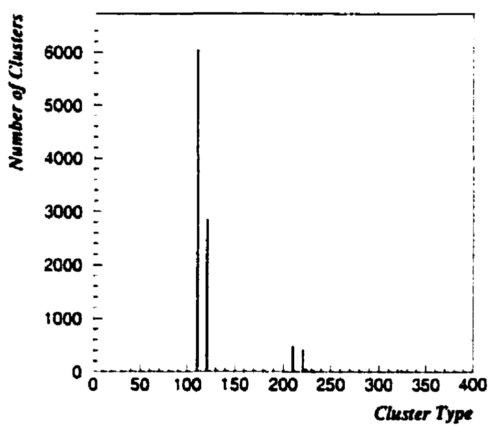

Figure 4.19: A typical distribution of types of reconstructed clusters in a cosmic ray test.

101) are found. Still, there is a significant number of clusters with 2 (or more) fired cells in both directions. This eventually contributes to the expansion of the pattern of fired cells outside the hit pattern, as mentioned above.

4.4.1 Detector Response as Function of Threshold

A systematic study of the detector behavior as a function of threshold have been done. All the other parameters remained fixed except threshold (HV= 1850 V, 50% Argon - 50% Ethane). Event statistics for different thresholds is shown in figure 4.20. One could notice that at high thresholds mainly 3 pads, reconstructed in one cells, are

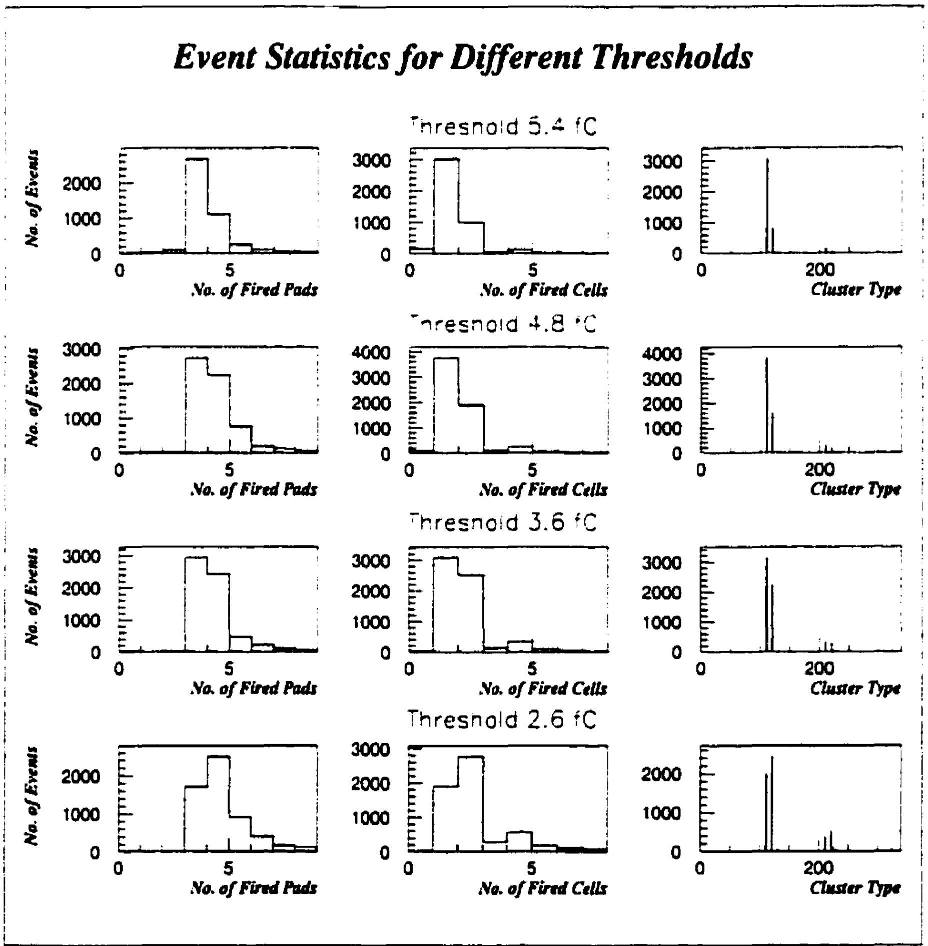

Figure 4.20: Event statistics as a function of threshold in cosmic ray tests ($HV = 1850\ V$).

fired. Gradually as the threshold is decreased, the events with 4 pads (reconstructed in 2 cells), become predominant. The number of "empty" events is relatively small and is decreasing as the threshold is reduced. This indicate a very good efficiency. This is confirmed in figure 4.21 where is presented the efficiency curve as a function of threshold. We get efficiencies close to 100% for thresholds below 4 fC. The chamber

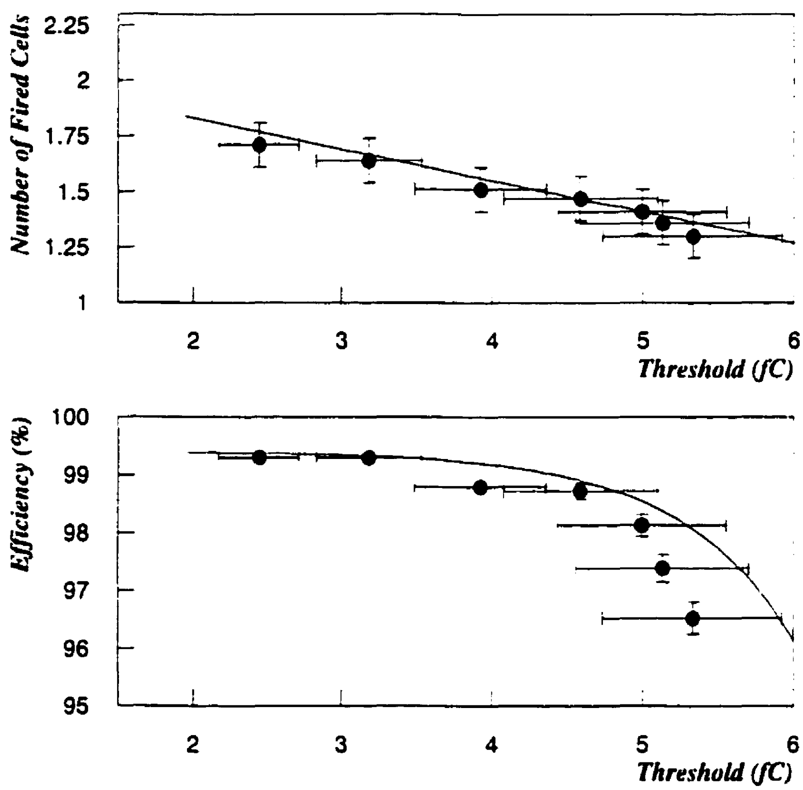

Figure 4.21: Average number of fired cells (**top**) and efficiency (**bottom**) as a function of the threshold value in cosmic ray tests ($HV = 1850V$).

operation is stable even for thresholds below 2 fC. Even at 4 fC the reconstructed clusters are not too big, an average of 1.5 fired cells per event is being registered.

4.4.2 Detector Response as Function of the Anode Bias

Similar results are expected to be obtained when we vary the anode bias while keeping a fixed threshold and gas mixture. The event statistics and efficiency curve as function of HV are presented in figure 4.22. The same good behavior and stability of the chamber is observed. As one could see, this time we get efficiencies close to 100% above about 1850 V (for a threshold of 3.9 fC). For the same threshold we need only 1700 V anode voltage in order to get efficiencies close to 100% in X-ray tests. This is due to the difference in charge deposit by the two kinds of particles (see figure 4.1).

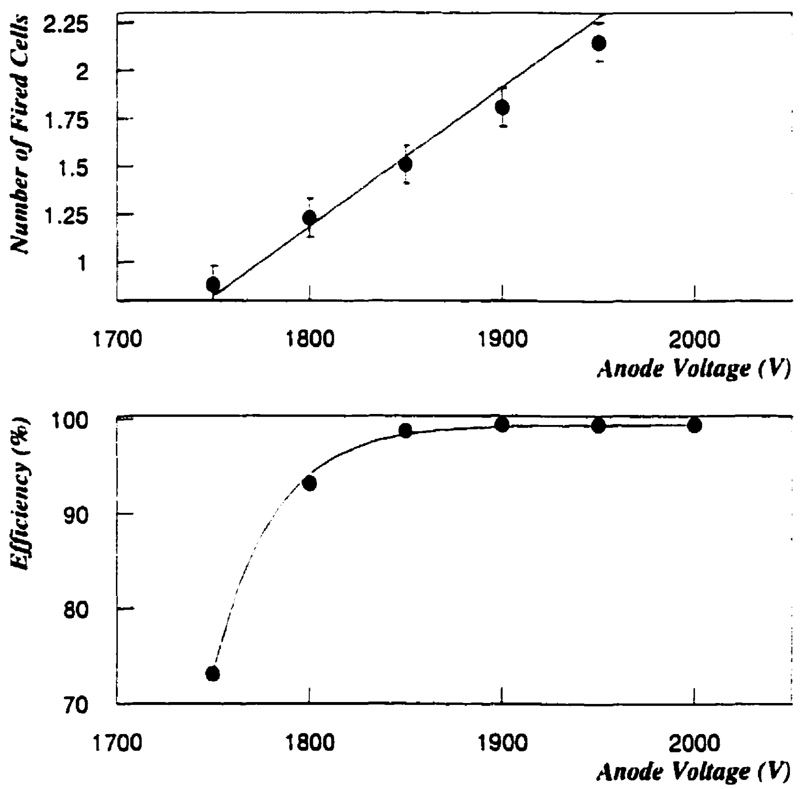

Figure 4.22: Average number of fired cells (**top**) and efficiency (**bottom**) as a function of the anode voltage in cosmic ray tests. ($\textit{Threshold} = 3.9\ fC$)

As discussed in section 4.3.2 only the ratio of the threshold and anode charge should be relevant in a region where the noise does not play an important role.

Equation 2.7 shows that the charge distribution is always proportional with the anode charge, and obviously the charge collected by the pads will keep the same feature. Therefore, it should be possible to plot simultaneously the results for both tests if we consider this ratio instead of the threshold and anode voltage. The anode charge is obtained from the fitting of the Landau distribution of the charge deposited by incident particles (see figure 4.15). The most probable value is kept for the calculation. Figure 4.23 shows, within experimental errors, a very good agreement between the two kinds of tests.

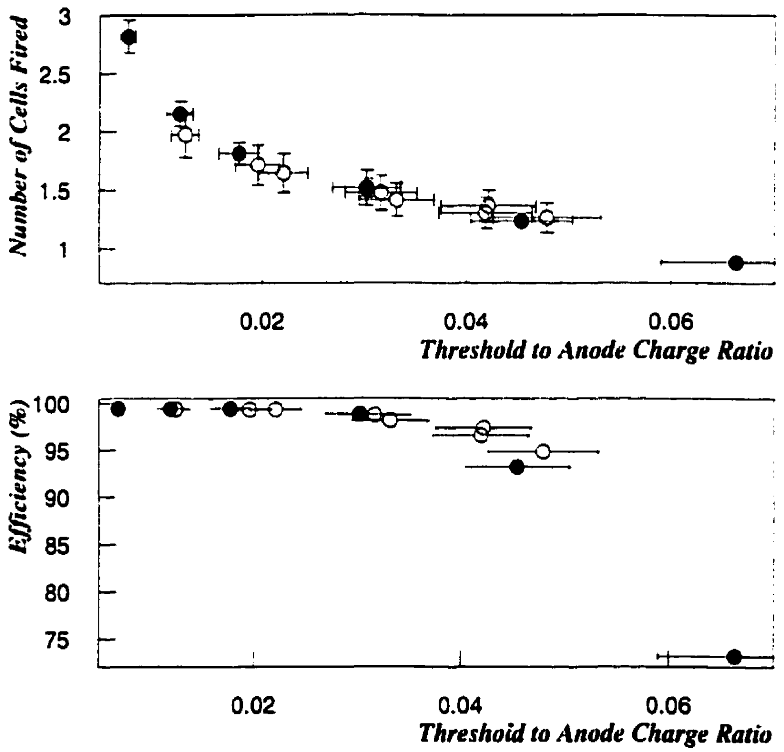

Figure 4.23: Comparison between the cosmic ray data obtained by varying the anode voltage and threshold. The **top** figure represents the average number of fired cell per event. Empty circles ("o") shows data where the threshold is varied while the anode voltage is kept constant. Full circles ("•") correspond to the test with the anode voltage as variable. The **bottom** figure shows the corresponding efficiency.

We have obtained good data in all experiments. The tests were done over a long period of time, the results being stable and consistent with each other. In the next chapter we will try to see if we can understand the results by simulation calculations.

Chapter 5

Simulations

The model for comparison calculations are based on the pad chamber simulation software developed for the PHENIX experiment mainly by M. Rosati, K. Filimonov and J.T. Mitchell.

5.1 Simulation Program Flow

A flowchart of the simulation program is shown in figure 5.1. The entry/exit co-

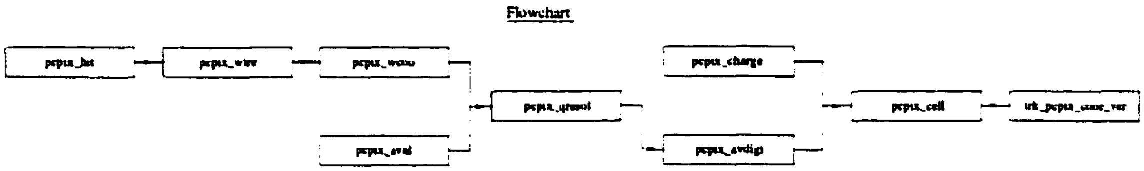

Figure 5.1: Flowchart of the simulation program.

ordinates are randomly produced, between some specified limits, in the *subroutine pcpix_hit*. For simulation of the cosmic ray data the limits are set so that we reproduce the active area defined by the three scintillators (see figure 4.13). The angular distribution of the cosmic rays is considered to be uniform, the incident angle being restricted only by the geometry of the trigger detectors. From the entry/exit coordinates the *subroutine pcpix_wire* calculates the detector cell(s) traversed by the incident particle as well as the number of the correspondent anode wire(s). The *Subroutine pcpix_wcoo* determines the cell number and the relative position along the wire corresponding to the hit. Then the *subroutine pcpix_aval* simulates the Landau shape of the anode charge distribution. The *function pcpix_charge* calculates the charge on individual pixels taking into account the position of the avalanche and pixels. The induced charge distribution is given by the single parameter empirical formula 2.9 and adjusted to take into account the field wires. *Subroutine pcpix_avdigi* calculates the charge collected by individual pads by summing the charge on component pixels. Once the charge on pads is known *subroutine pcpix_qresol* smears charge on pads with noise. Then the charge on individual pads is compared with the threshold of the discriminator and a reconstruction of fired cells is made by *subroutine pcpix_cell.* Once the arrays of fired cells is completed the cluster reconstruction is done by *subroutine trk_pcpix_coor_ver.*

5.2 Contribution of Electronic Noise

An important parameter in the simulation calculations is the contribution of electronic noise. A study of the effect of this noise has been done. For this a random trigger, provided by a pulser, was used as primary LEVEL 1 signal. The fraction of events with channel fired was recorded as function of threshold for different pad-channels. The results for the sixteen channels of one TGLD chips is shown on the left side of figure 5.2, in linear and logarithmic scales. The results are very similar for all channels except for one noisier channel, which shows the same behavior for thresholds higher with approx. $0.5 - 0.7\ fC$. The number of firings goes down almost linearly between $0.4 - 1\ fC$ then decrease abruptly. Practically above $1.5\ fC$ there are no more channels firing on noise. The figures on the right shows the simulation results. Here it is useful to recall figure 3.7. In that figure one sees the main feature of the noise superposed on the discriminator output. If we change the time scale we

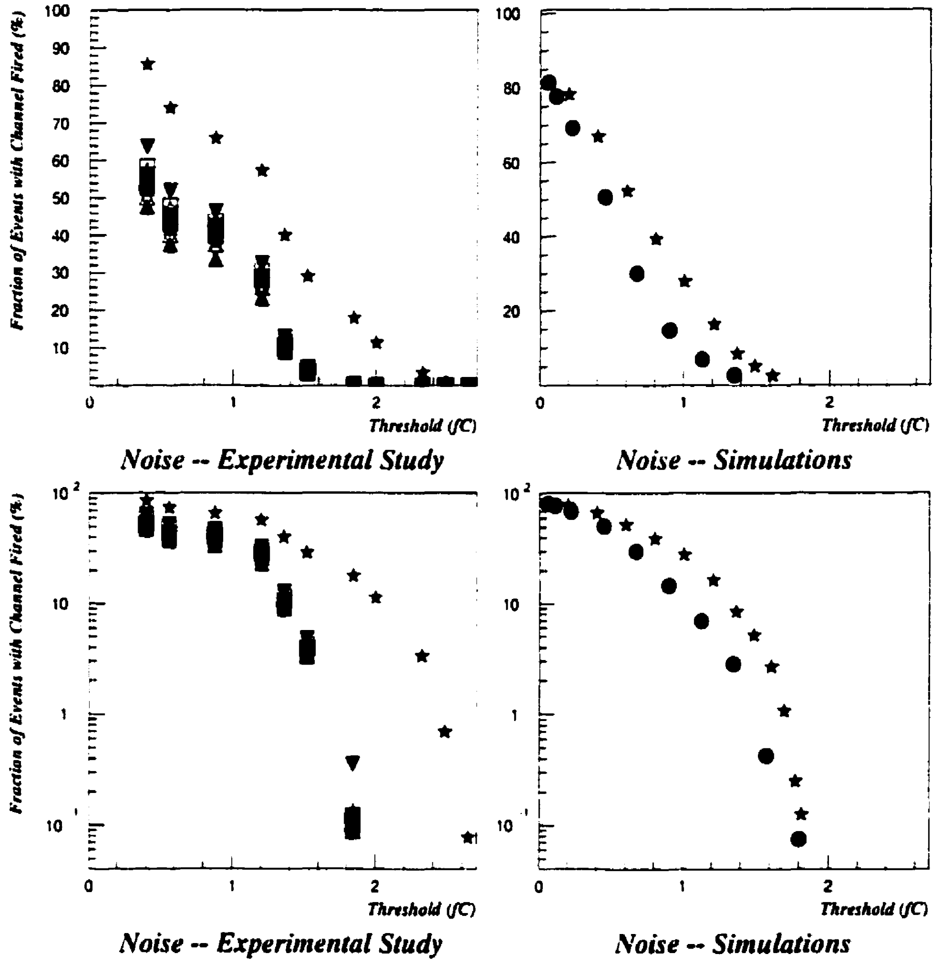

Figure 5.2: Fraction of events with fired channel as a function of threshold. Experimental and simulation data are presented on linear and logarithmic scale. The left figures show the experimental data for the 16 channels of one TGLD chip (each marker type label one different channel). The right figures show the result of simulations using a Gaussian shape ($\bullet$) and a sinusoidal shape ($\star$) noise.

notice that the noise oscillations we see in this picture are in fact due to amplitude variation of a 100 MHz oscillation. We see that our noise effect is very similar with that produced by a TV broadcast. This is not very surprising since the Montreal main TV-antenna on Mont-Royal is located less than 1 km away and in direct view of our laboratory. This is a particularly disadvantageous situation not expected to be encountered in the real experiments were the detectors are screened. We have tried to use aluminum foils to screen the detector and ferrite snaps around the cables to impinge the RFM noise pick-up. There was a noticeable improvement, the detector noise pick-up being acceptable as shown by our results. Once this noise is removed we expect the detector noise to be significantly smaller than in the present test.

It should be remembered that the discriminator triggering in the TGLD will in fact not be determined by the average value of the noise but is expected to be determined by the maximum value of the noise signal during the duration of the discriminator gate (125 ns). The shape of the electronic noise described above suggests two ways of modeling the noise contribution to the TGLD output. The noise contribution for a random LEVEL 1 trigger was generated using the Monte Carlo technique with the following functions:

Gaussian Model: Here we assume $Q^1_{noise} = P_1 + q_x$, where q_x can have any value from $-\infty$ to $+\infty$ with Gaussian probability $Pr_1(x) = exp(-\frac{q_x^2}{2 * P_2^2})$. In this model we assume that there is a variation around a mean value (P_1). The probability decrease exponentially as the absolute difference with the mean increase.

Sinus Model: Here we assume $Q^2_{noise} = P_1 + P_2 q_x$. We randomly generate the variable x between $(-\frac{\pi}{P_3} : +\frac{\pi}{P_3})$. Then $q_x(x) = \cos P_3 x$. This is an approximation for the noise generated by a radio broadcasting, which is a superposition of sinusoidal frequencies. Our events come randomly in time related with this radio waves. The modulation frequency should be at least an order of magnitude larger than the readout timeslice (125ns).

A good description of the experimental data is given if we consider the noise distributions to have the parameters: $P_1 = 0.6\ fC$ and $P_2 = 0.6\ fC$ for the Gaussian fit, and $P_1 = 0.6\ fC$, $P_2 = 0.8\ fC$ and $P_3 = 0.5$ for the sinusoidal fit. The results of both models are close for relatively low and high thresholds. A slightly better description in the region 0.7 – 1.5 fC is given by the sinusoidal model.

Another question arise regarding the noise. Is the noise correlated between the various channels? If the noise is due to the electromagnetic interference it is expected to be highly correlated. If the noise is mainly thermal noise then it is expected to be mainly uncorrelated noise. Figure 5.3 shows the distribution of the number of fired pads per event for two runs in "noise" tests. Two thresholds settings are presented: a

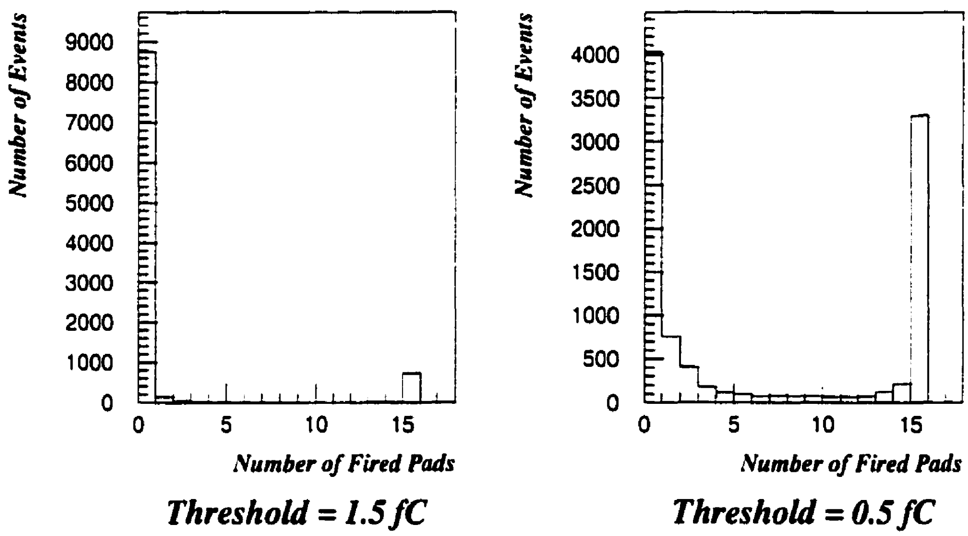

Figure 5.3: Study of the Noise Correlation. Experimental data showing the distribution of the number of fired pads per event for one TGLD chip. The **left** figure is for a 1.5 fC threshold. The **right** figure is for 0.5 fC. The first channel corresponds to no channel fired.

very low threshold 0.5 fC and a higher threshold of 1.5 fC. One chip (16 channels) is tested and its threshold is gradually decreased. The other chips are operated at normal threshold settings. One channel is dead in this chip. One could see that, most of the time, no pad is fired or all the pads are fired. For lower thresholds there are some individual channels triggering due to some differences in the channels noise or threshold. Still, there are clearly two peaks at 0 and 15, corresponding to all the active channels of the tested chip. Thus a fully correlated noise seems to be a reasonable assumption. This was our assumption in the present calculations.

5.3 Comparison of Simulation and Experimental Data

With these assumptions we try to simulate the behavior of the detector and to compare with the experimental data. We normalize the calculations to the most probable anode charge. First we try to compare the distribution of the fired pads, distribution of fired cells and the types of reconstructed clusters. Figure 5.4 show this comparison for the threshold to anode charge ratio 0.03, a normal threshold for operation with

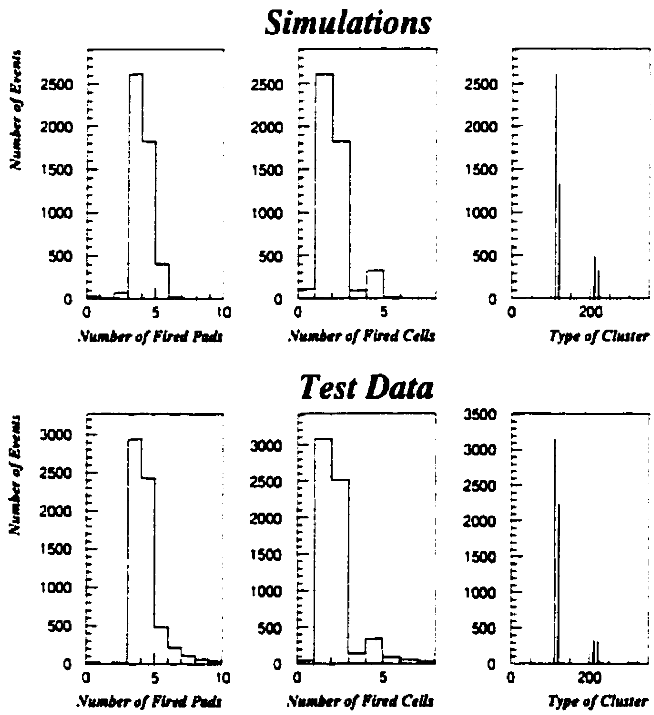

Figure 5.4: Comparison of the simulation calculations with test data. The distribution of fired pads and cells, and types of reconstructed clusters are shown. The threshold to the most probable anode charge ratio is 0.03.

a high efficiency (close to 100%) and small cluster dimensions ($1-1.5$ fired cells in average). The test data are from a run with $HV = 1850\ V$ and threshold $3.9\ fC$. For both, data and simulation, three pads are fired most of the time (reconstructed in one cell, cluster type#110). The pad distribution is very similar except for a longer tail in the test data for the pads and cells distribution. This could be a result of the outstanding noisy channels who trigger on noise and are not included in the simulation that assume equal noise contribution. The fired cell distribution have a very interesting feature, being present in both test and simulation data: for large anode charge events there are rather four cell clusters than clusters composed by three cells. This is a feature of our pixel-pad pattern (see sec. 2.6). With this specific pattern, if five pads are fired, there are in fact more combinations leading to a four cell cluster rather than a three cell cluster. The reconstructed cluster type distribution is similar to that measured, showing that most of the time clusters with one cell in x direction are observed. Cluster type#110 (one cell in z direction) is dominating over type#120 (two cells in z direction). There is a relatively small number of events with two cell clusters in the x direction. Figure 5.5 shows the same distributions for a threshold to anode charge ratio about three times lower. Again we observe a very good agreement

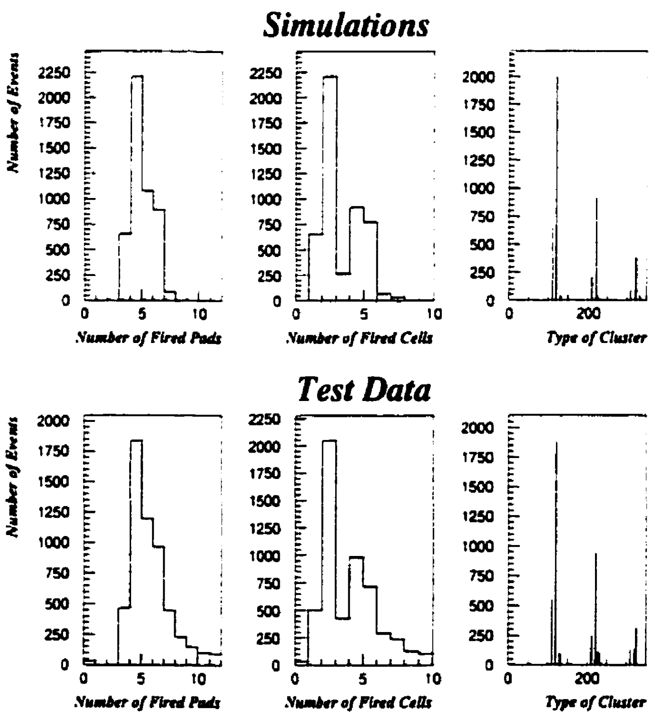

Figure 5.5: The distribution of fired pads and cells, and types of reconstructed clusters are shown. The threshold to the most probable anode charge ratio is 0.01.

between the test and simulation data. The same particular feature of the fired cells distribution can be noticed in both test and simulation data. We are seeing now that five cells clusters are more likely to be encountered than three cell clusters. The cluster type#120 is now appearing more often than type#110. The number of the clusters with two and three fired cells in x direction (type#2XX and #3XX) have increased significantly.

We have also calculated the efficiency and the average number of fired cells as a function of the threshold settings. Figure 5.6 displays these results plotted together with the experimental data. A very good agreement is observed for the average

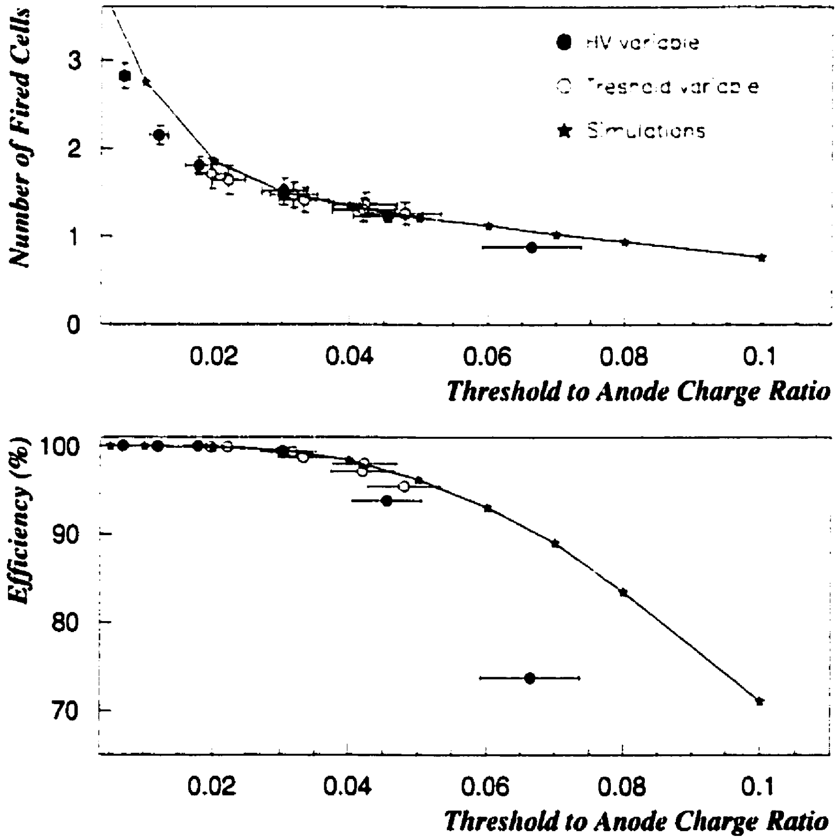

Figure 5.6: Simulation results compared with experimental data. The **top** figure show the average number of fired cells per event as function of threshold / most probable anode charge. The **bottom** figure shows the efficiency curve. Simulations are shown by symbols "⋆". Experimental data are indicated by "o" and "•".

number of cells fired. The slight enhancement, for thresholds lower than 0.02, could be the result of the dead or switched off channels. At these threshold settings there is a significant number of large clusters. Let's recall the way we have done the analysis (see section 4.2). If a cluster is found we do not search any more if other cells (with 1 dead pad) could have been fired. Therefore, it is possible for us to detect smaller clusters than under normal conditions with no dead pads. The efficiency curve is also well explained by the simulations for low thresholds. The test curve decrease faster than our model for thresholds higher than 0.05. Again this could be an effect of the variation of thresholds from channel to channel, never tested for the present prototype.

As a whole, the simulations results are in very good agreement with the experimental data. This gives us sufficient confidence to trust the predictions of the simulations for other parameters not tested in the present thesis (e.g.:position resolution).

Chapter 6

Conclusions and Summary

We have described the design, development and performance of a new prototype of MWPC with pixel pad cathode readout. This R&D work, carried out at McGill University, is part of the development of the tracking system to be used in PHENIX experiment under construction at Brookhaven National Laboratory.

Prototypes of pad chambers based on interpolating cathode pad (of chevron type) have been built at McGill prior to the present prototype. Although they offered a good position resolution, the high cost of an analog readout of such configuration imposed the need of a new design of the cathode board and the implementation of a digital readout. This need was fulfilled by the new design which consists of a pixel-pad pattern, where three pixels form a cell (the basic unit of the reconstruction). Nine pixels are linked together to form a pixel-pad in a specific manner. In this pixel-pad pattern any cell is formed by three pixels correspondent to a unique combination of three different pixel-pads. This configuration offers the attractive possibility to cope with the eventuality of dead channels. In this configuration the number of readout channels is reduced by a factor of almost three. Each pad has its own readout. For this, a new readout card (ROC) was designed, built and tested on a new prototype pad chamber in collaboration with Lund University and Oak Ridge National Laboratory. It consists of three 16-channel preamplifier/shaper/discriminator integrated CMOS chips (called TGLD) with adjustable threshold which digitize the charge collected by 48 pixel-pads. A digital memory unit (DMU), which is similar to a pipeline with variable length, stores the data until a trigger decision is made. Three TGLDs, a DMU and two interface chips are mounted on the readout cards using chip-on-board (COB) technology.

The tests of the prototype and its new electronics were done at McGill University over a period of one year. Systematic studies of the performance and efficiency of the chamber were done as function of the operating parameters of the chamber in tests with x-rays and cosmic rays. The cosmic ray tests offer an environment close to that expected in the PHENIX experiment. The distribution of the number of fired cathode pads and cells, and the detector efficiency were studied. The prototype shows very good stability. No change in chamber behavior was noticed during the long period of testing and consistent results were obtained. The tested chamber showed stable operation even for thresholds below 2 fC (corresponding to $1 - 1.5\%$ of the most probable anode charge, produced at 1850 V by a minimum ionizing particle) with reasonable noise contribution. A good stability is observed up to an anode voltage of 2100 V. Efficiencies above 99% were attained for threshold settings lower than about 4 fC and anode voltage of 1850 V, far from the limiting operating parameters of the chamber. Even for a low threshold of 4 fC the clusters were small in size (about 1.5 cells fired per event), leading to an expected particle resolution less than the cell size and a good two particle separation. All these will successfully fulfill the PHENIX requirements.

The chamber behavior was simulated using a Monte Carlo technique. The calculations take into consideration the electronic noise contribution and the geometry of the trigger detectors. They assume the Landau shape, of the anode charge spectrum, with the parameters obtained from the fit of the experimental data. The induced charge distribution is obtained by using an empirical formula from which the induced charge on each pixel is calculated. An excellent description of chamber behavior was obtained, showing that we can use these simulations to predict and optimize the performance of such chamber.

Bibliography

[1] J. Rafelski and B. Müler, Phys. Rev. Lett. **48**, 1066 (1982).

[2] C. M. Hung and E. V. Shuryak, Phys. Rev. Lett. **75**, 4003 (1995).

[3] PHENIX Collaboration, *Preliminary conceptual design report* (Brookhaven National Laboratory, New York, USA, 1992).

[4] J. D. Bjorken, Phys. Rev. **D27**, 140 (1983).

[5] C-Y. Wong, *Introduction to high-energy heavy-ion collisions* (World Scientific, Singapore, 1994), p. 17.

[6] E. V. Shuryak, Phys. Lett. **B78**, 150 (1978).

[7] I. Tserruya, Nucl. Phys. **A590**, 126 (1995).

[8] R. Hwa, K. Kajantie, Phys. Rev. **D32**, 1109 (1985).

[9] K. Kajantie, J. Kapusta, L. McLerran, A. Mekjian, Phys. Rev. **D34**, 2746 (1986).

[10] G.E. Brown, M. Rho, Phys. Rev. Lett. **66**, 2720 (1991).

[11] R. Pisarski, Phys. Lett. **B110**, 155 (1982).

[12] J. D. Bjorken, Acta Phy. Polon. **B23**, 637 (1992).

[13] U. Heinz, K. S. Lee, Phys. Lett. **B259**, 162 (1991).

[14] R. Hwa, K. Kajantie, Phys. Rev. Lett **68**, 3270 (1992).

[15] P. C. [3], 16 .

[16] W. Blum. L. Rolandi. *Particle Detection with Drift Chambers* (Springer-Verlag, Berlin. 1993).

[17] R. Evans. *The Atomic Nucleus* (McGraw-Hill, Inc., New York. USA, 1955).

[18] R. Veenhof. *Garfield, a drift chamber simulation program* (CERN program library entry W5050. Geneva. Switzerland. 1991).

[19] W. Raether. *Electron avalanches and breakdown in gases* (Butterworths, Washington, USA. 1964).

[20] H. Okuno. J. Fisher. V. Radeka and H. Walenta. IEEE Trans. Nucl. Sci. **NS-26**, 160 (1979).

[21] B. Yu. Ph.D. thesis. University of Pittsburgh, 1991.

[22] V.Radeka. Ann. Rev. Nucl. Part. Sci. **38**. 271 (1988).

[23] I. Endo et al., Nucl. Instr. and Meth. **178**. 543 (1980).

[24] E. Gatti. A. Longoni, H. Okuno, Nucl. Instr. and Meth. **163**. 83 (1979).

[25] J. S. Gordon and E. Mathieson, Nucl. Instr. and Meth. **227**. 267 (1984).

[26] J. R. Thompson. J. S. Gordon and E. Mathieson, Nucl. Instr. and Meth. **A234**, 505 (1985).

[27] J. S. Gordon and E. Mathieson, Nucl. Instr. and Meth. **227**, 277 (1984).

[28] E. Mathieson, Nucl. Instr. and Meth. **A270**, 602 (1988).

[29] Bo Yu [21], 25 .

[30] Bo Yu [21], 25 .

[31] J. L. Alberi and V. Radeka, IEEE Trans. Nucl. Sci. **NS-23**, 251 (1976).

[32] A. L. S. Angelis et al., Nucl. Instr. and Meth. **A283**, 762 (1976).

[33] G. C. Smith, J. Fisher, V. Radeka, IEEE Trans. Nucl. Sci. **NS-35**, 409 (1988).

[34] E. Mathieson and G. C. Smith, IEEE Trans. Nucl. Sci. **NS-36**, 305 (1989).

[35] O. H. W. Siegmund et al., IEEE Trans Nucl. Sci. **NS-30**, 503 (1983).

[36] R. Allemand and G. Thomas, Nucl. Instr. and Meth. **137**, 141 (1976).

[37] D. F. Anderson, H. K. Arvela, A. Breskin and G. Charpak, Nucl. Instr. and Meth. **224**, 315 (1984).

[38] T. Mikki, R. Itoh and T. Kamae, Nucl. Instr. and Meth. **A236**, 64 (1985).

[39] J. Fisher et al., IEEE Trans. Nucl. Sci. **NS-37**, 82 (1990).

[40] H. O. Anger, Instr. Soc. Am. Trans. **5**, 311 (1966).

[41] B. Yu, G. C. Smith, V. Radeka and E. Mathieson, IEEE Trans. Nucl. Sci. **NS-38**, 454 (1991).

[42] Bo Yu [21], 69 .

[43] J. Barrette et al., Nucl. Instr. and Meth. **A385**, (1997).

[44] D. Gan, Master's thesis, McGill University, 1996.

[45] R. Debbe et al., Nucl. Instr. and Meth. **A283**, 772 (1989).

[46] R. Debbe et al., IEEE Trans. on Nucl. Phys. **NS-37**, 88 (1990).

[47] Bo Yu [21], 46 .

[48] Particle Data Group, Physical Review **D50**, 1251 (1994).

[49] Application Software Group, *PAW-Physics Analysis Workstation 2.03* (CERN Program Library, Geneva, Switzerland, 1993).